Inorganic Chemistry

pubs.acs.org/IC

Article

# Hypoxia-Active Iridium(III) Bis-terpyridine Complexes Bearing Oligothienyl Substituents: Synthesis, Photophysics, and Phototoxicity toward Cancer Cells

Xinyang Sun,[†] Houston D. Cole,[†] Ge Shi, Victoria Oas, Alisher Talgatov, Colin G. Cameron, Svetlana Kilina, Sherri A. McFarland,* and Wenfang Sun*

Cite This: *Inorg. Chem.* 2024, 63, 21323−21335

Read Online

ACCESS | Metrics & More | Article Recommendations | Supporting Information

**ABSTRACT:** In an effort to develop hypoxia-active iridium(III) complexes with long visible-light absorption, we synthesized and characterized five bis(terpyridine) Ir(III) complexes bearing oligothienyl substituents on one of the terpyridine ligands, i.e., ***n*T-Ir** ($n$ = 0−4). The UV−vis absorption, emission, and transient absorption spectroscopy were employed to characterize the singlet and triplet excited states of these complexes and to explore the effects of varied number of thienyl units on the photophysical parameters of the complexes. *In vitro* photodynamic therapeutic activities of these complexes were assessed with respect to three melanoma cell lines (SKMEL28, A375, and B16F10) and two breast cancer cell lines (MDA-MB-231 and MCF-7) under normoxia (∼18.5% oxygen tension) and hypoxia (1% oxygen tension) upon broadband visible (400−700 nm), blue (453 nm), green (523 nm), and red (633 nm) light activation. It was revealed that the increased number of thienyl units bathochromically shifted the low-energy absorption bands to the green/orange spectral regions and the emission bands to the near-infrared (NIR) regions. The lowest triplet excited-state lifetimes and the singlet oxygen generation efficiency also increased from **0T** to **2T** substitution but decreased in **3T** and **4T** substitution. All complexes exhibited low dark cytotoxicity toward all cell lines, but **2T-Ir**−**4T-Ir** manifested high photocytotoxicity for all cell lines upon visible, blue, and green light activation under normoxia, with **2T-Ir** showing the strongest photocytotoxicity toward SKMEL28, MDA-MB-231, and MCF-7 cells, and **4T-Ir** being the most photocytotoxic one for B16F10 and A375 cells. Singlet oxygen, superoxide anion radicals, and peroxynitrite anions were found to likely be involved in the photocytotoxicity exhibited by the complexes. **4T-Ir** also showed strong photocytotoxicity upon red-light excitation toward all cell lines under normoxia and retained its photocytotoxicity under hypoxia toward all cell lines upon visible, blue, and green light excitation. The hypoxic activity of **4T-Ir** along with its green to orange light absorption, NIR emission, and low dark cytotoxicity suggest its potential as a photosensitizer for photodynamic therapy applications.

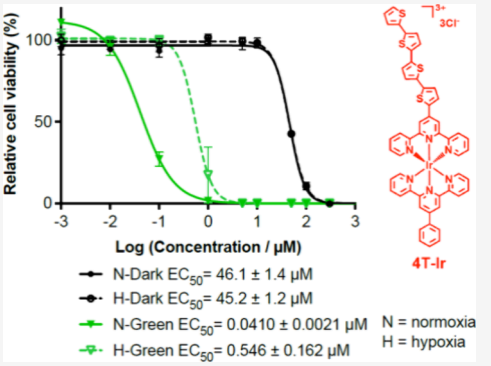




## INTRODUCTION

Transition-metal complexes have been a center of attention in fields ranging from optoelectronics to photovoltaics for more than several decades now.[1−5] Their highly tunable electronic properties have been exploited for not only luminescence imaging and solar energy conversion but also in photoredox catalysis.[6] More recently, they have emerged as promising systems for medicinal applications such as photodynamic therapy (PDT) and photoactivated chemotherapy (PACT).[7−15] The ruthenium(II) complex TLD1433 is one example and has advanced to Phase 2 clinical trials for treating bladder cancer (ClinicalTrials.gov Identifier: NCT03945162).[10] Although Ru(II) may in fact be the most widely studied transition metal for its properties and potential applications,[16] iridium(III) is quickly gaining interest.

Ir(III) complexes are also attractive transition-metal complexes for photonic and biophotonic applications and have potential as photosensitizers (PSs) for PDT.[12−15] The heavy Ir(III) ion facilitates intersystem crossing to populate the lowest-energy triplet excited state ($T_1$) that sensitizes singlet oxygen and other reactive molecular species (RMS). There is considerable interest in PSs that can be activated by tissue-penetrating near-infrared (NIR) light and remain active under hypoxia. The latter can render PDT ineffective due to its reliance on oxygen and the fact that the PDT process itself can cause tissue to become hypoxic. Long-lived $T_1$ states are particularly attractive since they may enable sensitization of singlet oxygen and other reactive oxygen species (ROS) even

**Received:** September 10, 2024
**Revised:** October 5, 2024
**Accepted:** October 11, 2024
**Published:** October 23, 2024

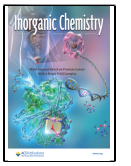

**Scheme 1. Synthetic Route and Structures for Ir(III) Complexes 0T-Ir−4T-Ir**

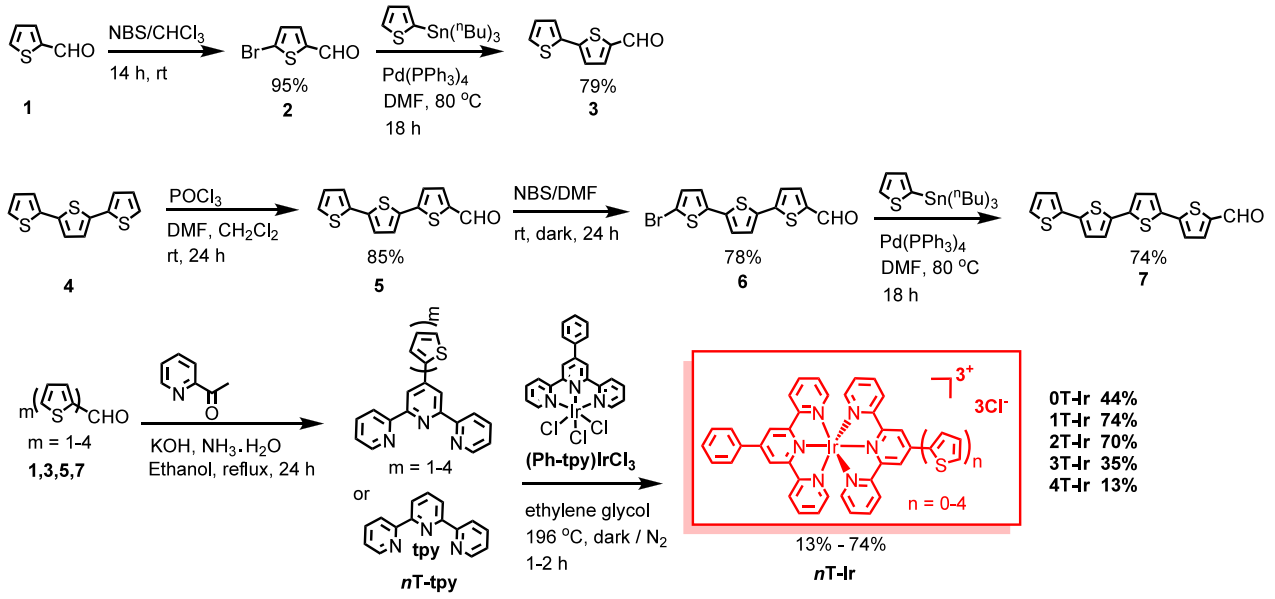


at low oxygen tension or act via oxygen-independent pathways. Most Ir(III)-based PSs that have been reported absorb shorter wavelength UV to blue light and lose their photocytotoxicity under hypoxia.[12−15] Longer visible to NIR light absorbing and hypoxia-active Ir(III) PSs are quite scarce.[17−20]

A majority of the published Ir(III) PSs contain tris-bidentate ligands.[12−15] Although the tris-bidentate geometry may provide greater structural diversity and can be prepared under mild reaction conditions, the presence of stereoisomers can be problematic.[21−27] In contrast, bis-terdentate Ir(III) complexes containing symmetric terdentate ligands, such as terpyridine (tpy), do not exhibit stereoisomerism like their tris-bidentate counterparts, preventing the complication in the separation of different stereoisomers. In addition, the mononuclear bis-tpy Ir(III) complexes ($[Ir(tpy)_2]^{3+}$) have +3 charges compared to their Ru(II)/Os(II) bis-tpy counterparts having +2 charges and the widely studied monocationic biscyclometalated $[Ir(C^N)_2(N^N)]^+$ (C^N refers to the cyclometalating ligands and N^N refers to the diimine ligands) complexes. The higher charge increases the water solubility, making them more suitable for bioapplications. However, bis-terdentate Ir(III) complexes are far less developed in comparison due to the harsher reaction conditions for synthesizing them.

Our past work investigated the PDT effects of mononuclear and dinuclear bis-tpy Ir(III) complexes toward melanoma cells or lung cancer cells and toward MCF-7 breast tumors.[28−30] We found that $\pi$-expansive pyrenyl (pyr) substituents appended to one of the tpy ligands extended the lifetime of the $T_1$ state from 2.25 to 5.79 $\mu$s and increased the singlet oxygen quantum yield from 14% to 81%. These systems were phototoxic to SKMEL28 melanoma cells in the submicromolar regime using broadband visible light (400−700 nm), with phototherapeutic indices (PIs) > 10.[3,29] $[Ir(Ph\text{-}tpy)(pyr\text{-}tpy)]^{3+}$ induced effective tumor regression for mice bearing MCF-7 tumors upon blue light irradiation.[29] The dinuclear Ir(III) counterpart, end-capped with 4-phenylterpyridine ligands, was also phototoxic in the submicromolar regime with a PI on the order of $10^2$ toward SKMEL28 cells under similar conditions.[30] Although promising, the absorption of these bis-tpy Ir(III) complexes was limited to the blue spectral regions.

Our previous studies showed that the absorption of tris-bidentate Ir(III) complexes can be significantly red-shifted by introducing $\pi$-conjugated organic chromophores to the ligand that also switch the $T_1$ state to the long-lived $^3\pi,\pi^*$ state localized to the organic chromophore.[19,31,32] This strategy was also applied to shift the absorption of Ru(II) bis-tpy complexes into the green spectral region with boron dipyrromethene (BODIPY)-appended tpy ligands.[33] Unfortunately, the BODIPY unit cannot tolerate the high temperatures required for preparing the corresponding Ir(III) complexes. Thus, more heat-stable organic chromophores are needed to generate the Ir(III) bis-tpy systems.

For this, we turned to oligothiophenes, a key feature of TLD1433 that simultaneously red-shifted the ground-state absorption and prolonged the $T_1$ lifetime.[34−38] Herein, we append oligothienyl groups ($n$T, where $n$ = 0−4) to one of the tpy ligands and study the impact of the $\pi$-conjugation length on the photophysics and *in vitro* PDT effects toward melanoma and breast cancer cells under normoxia and hypoxia. These cell lines were selected because they represent cancers for which the clinical presentation of hypoxia is known and both cancers involve surgery as a standard of care whereby intraoperative PDT could be realized.

## EXPERIMENTAL SECTION

**Synthesis and Characterizations.** All of the reagents and solvents were obtained from commercial sources and used directly without further purification. Methanol was purchased from Fisher Scientific and different grades were used for different purposes: i.e., ACS grade for synthesis, HPLC grade for LC eluent, and Optima grade for sample preparation for HPLC and mass analyses. Deuterated solvents from Cambridge Isotope Laboratories were used for the NMR analyses. A Teledyne ISCO CombiFlash EZ Prep UV Preparative Flash Chromatograph System was used for carrying out flash column chromatography using SILICYCLE SiliaSep 25 g prepacked silica cartridges. The $^1$H NMR spectra in DMSO-$d_6$ were measured on a Bruker Ascend 500 spectrometer, and the spectra in $CD_3OD$ were measured on a JEOL 400 MHz spectrometer. High-resolution electrospray ionization ($ESI^+$) mass spectra were obtained


https://doi.org/10.1021/acs.inorgchem.4c03847
Inorg. Chem. 2024, 63, 21323−21335

on a Waters Xevo G2-XS QTof instrument. An Agilent/Hewlett-Packard 1100 series instrument with a Hypersil GOLD C18 reversed-phase column was used for HPLC analyses. Methanol solutions of **0T-Ir**−**4T-Ir** (100 μM) were injected, and the eluent varied from 98% of gradient A (0.1% formic acid in $H_2O$) mixed with 2% of gradient B (0.1% formic acid in $CH_3CN$) to 5% of gradient A mixed with 95% gradient B. The errors for the retention times are within ±0.1 min.

The synthetic route for complexes **0T-Ir**−**4T-Ir** is illustrated in Scheme 1. Compounds thiophene-2-carboxaldehyde (**1**), 2,2′:5′,2″-terthiophene (**4**), 2,2′:6′,2″-terpyridine (**tpy**), 2-(tributylstannyl)-thiophene, 2-acetylpyridine, and iridium(III) chloride trihydrate ($IrCl_3(H_2O)_3$) were purchased from VWR. Compounds 4′-phenyl-2,2′:6′,2″-terpyridine (**Ph-tpy**),[29] (**Ph-tpy**)$IrCl_3$,[29] 5-bromothiophene-2-carboxaldehyde (**2**),[39] (2,2′-bithiophene)-5-carboxaldehyde (**3**),[40] (2,2′:5′,2″-terthiophene)-5-carboxaldehyde (**5**),[41] 5″-bromo-(2,2′:5′,2″-terthiophene)-5-carboxaldehyde (**6**),[42] and (2,2′:5′,2″:5″,2‴-quaterthiophene)-5-carboxaldehyde (**7**)[40] were synthesized according to the literature procedures. Ligands **1T-tpy**−**4T-tpy** and the target complexes **0T-Ir**−**4T-Ir** were synthesized following the procedure reported by our group before[29] and were characterized via $^1$H NMR (Figures S1−S12 in the Supporting Information). **0T-Ir**−**4T-Ir** were further characterized via $^{13}$C and $^1$H−$^1$H COSY NMR (Figures S1−S5 and S8−S12 in the Supporting Information), ESI$^+$−MS (Figures S13−S17 in the Supporting Information), and HPLC (Figures S18−S22 and Table S1 in the Supporting Information). No uncommon hazards are noted.

*General Procedure for the Synthesis of* ***1T-tpy*** *−* ***4T-tpy.*** To a 250 mL round-bottom flask, compounds **1**, **3**, **5**, or **7** (1.0 equiv), 2-acetylpyridine (2.0 equiv), and ethanol were added followed by the addition of KOH (2.0 equiv). The resulting mixture was stirred at room temperature for 2 h. Then, ammonium aqueous solution (28% (w/v), 5.0−20.0 equiv) was added into the reaction mixture and the mixture was refluxed for 24 h. After the reaction mixture was cooled to room temperature, the precipitate was filtered out, washed with water and ethanol, and then air-dried. **1T-tpy**, **2T-tpy**, and **4T-tpy** were directly used for the complexation with (**Ph-tpy**)$IrCl_3$ without further purification, while **3T-tpy** was recrystallized in ethanol.

*4′-(Thiophen-2-yl)-2,2′:6′,2″-terpyridine (**1T-tpy**).* Thiophene-2-carboxaldehyde (**3**) (1.12 g, 10.0 mmol), 2-acetylpyridine (2.42 g, 20.0 mmol), ethanol (100 mL), KOH (1.12 g, 20.0 mmol), and ammonium aqueous solution (28%) (6.9 mL, 50.0 mmol) were used. The product obtained was an off-white solid (1.3 g, yield: 41%), which was used for the complexation reaction directly. $^1$H NMR (400 MHz, $CDCl_3$) δ: 8.77 (m, 4 H), 8.69 (d, 2H), 7.95 (m, 2H), 7.88 (m, 1H), 7.46 (m, 1H), 7.42 (m, 2H), 7.19 (m, 1H).

*4′-((2,2′-Bithiophen)-5-yl)-2,2′:6′,2″-terpyridine (**2T-tpy**).* (2,2′-Bithiophene)-5-carboxaldehyde (**5**) (800 mg, 4.12 mmol), 2-acetylpyridine (997 mg, 8.24 mmol), ethanol (100 mL), KOH (462 mg, 8.24 mmol), and ammonium aqueous solution (28%) (5.8 mL, 41.2 mmol) were used. The product obtained was a yellow solid (400 mg, yield: 24%) and used for the complexation reaction directly.

*4′-((2,2′:5′,2″-Terthiophen)-5-yl)-2,2′:6′,2″-terpyridine (**3T-tpy**).* (2,2′:5′,2″-Terthiophene)-5-carboxaldehyde (**5**) (276 mg, 1.0 mmol), 2-acetylpyridine (242 mg, 2.0 mmol), KOH (112 mg, 2.0 mmol), ethanol (20 mL), and ammonium aqueous solution (28%) (2.8 mL, 20.0 mmol) were used. After washing with water and ethanol, the obtained solid was recrystallized from ethanol, and the product was obtained as a yellow solid (280 mg, yield: 58%). $^1$H NMR (400 MHz, $CDCl_3$) δ 8.78 (d, *J* = 4.4 Hz, 2H), 8.70 (s, 2H), 8.68 (d, *J* = 8.0 Hz, 2H), 7.91 (td, *J* = 1.7, 7.6 Hz, 2H), 7.74 (d, *J* = 3.8 Hz, 1H), 7.39 (td, *J* = 0.4, 5.3 Hz, 2H), 7.27 (t, *J* = 3.9 Hz, 2H), 7.23 (d, *J* = 2.5 Hz, 1H), 7.21 (d, *J* = 3.8 Hz, 1H), 7.15 (d, *J* = 3.8 Hz, 1H), 7.07 (q, *J* = 3.5 Hz, 1H).

*4′-((2,2′:5′,2″:5″,2‴-Quaterthiophen)-5-yl)-2,2′:6′,2″-terpyridine (**4T-tpy**).* (2,2′:5′,2″:5″,2‴-Quaterthiophene)-5-carboxaldehyde (**7**) (235 mg, 0.64 mmol), 2-acetylpyridine (155 mg, 1.28 mmol), KOH (71.7 mg, 2.0 mmol), ethanol (20 mL), and ammonium aqueous solution (28%) (1.8 mL, 12.8 mmol) were used. The product obtained was a brown solid (250 mg, yield: 69%), which was used for the complexation reaction directly.

*General Procedure for the Synthesis of* ***1T-Ir*** *−* ***4T-Ir.*** Compounds (**Ph-tpy**)$IrCl_3$ (1.0 equiv) and ***n*T-tpy** (*n* = 0−4) (1.0 equiv) were added to a 50 mL nitrogen flushed round-bottom flask, and ethylene glycol (5.0−10.0 mL) was then added. The resulting mixture was refluxed under nitrogen in the dark for 1 h. When the reaction mixture was cooled to room temperature, an aqueous solution of $NH_4PF_6$ (0.25 M, 10.0 equiv) was added into the reaction solution and stirred at room temperature for 2 h. The precipitate was collected by filtration and washed with distilled water. Then, the solid was disbursed in methanol and $NH_4Cl$ (30.0 equiv) was added. The resulting mixture was stirred overnight at room temperature. After the solid was filtered out, the solvent in filtrate was removed under vacuum and the residue was washed with water to remove the remaining salt. The obtained crude product was purified on an alumina (basic) column using $CH_2Cl_2$/$CH_3OH$ (100:0−100:10 (v/v)) as the eluent. The product was then further purified on the Teledyne ISCO CombiFlash EZ Prep Chromatograph System using a silica gel flash column chromatography cartridge with a gradient of $CH_3CN$ to 10% water in $CH_3CN$ followed by 7.5% water in $CH_3CN$ with 0.5% $KNO_3$. The dark red product-containing fractions that were eluted only in the presence of $KNO_3$ were then combined and concentrated under vacuum, then transferred to a separatory funnel with $CH_2Cl_2$ (25 mL), deionized water (25 mL), and saturated aqueous $KPF_6$ (1 mL). The resulting mixture was gently agitated, and the $CH_2Cl_2$ layer was drained. Additional $CH_2Cl_2$ (2 × 25 mL portions) was used to extract the remaining product until the aqueous layer was colorless. The $CH_2Cl_2$ layers were then combined, dried under vacuum, and then converted to the corresponding $Cl^-$ salt in quantitative yield by eluting the samples through a column of Amberlite IRA-410 with MeOH as the eluent. The complexes were then collected and dried under reduced pressure. The product was a powder with a color from yellow to orange to dark red as the number of thiophene rings increased on the tpy ligand. The yields varied from 13% to 74%.

*0T-Ir.* Compounds (**Ph-tpy**)$IrCl_3$ (260 mg, 0.429 mmol), **tpy** (100 mg, 0.429 mmol), and ethylene glycol (19.0 mL) were used. The product obtained was a pale-yellow powder (160 mg, yield: 44%). $^1$H NMR (500 MHz, DMSO-$d_6$): δ 9.67 (s, 2H), 9.33−9.28 (m, 4H), 9.02 (d, *J* = 8.0 Hz, 2H), 8.93 (t, *J* = 8.2 Hz, 1H), 8.51 (d, *J* = 8.0 Hz, 2H), 8.37 (td, *J* = 7.9, 1.5 Hz, 2H), 8.33 (td, *J* = 7.9, 1.4 Hz, 2H), 7.97 (dd, *J* = 5.7, 1.3 Hz, 2H), 7.85 (dd, *J* = 5.8, 1.4 Hz, 2H), 7.83 (t, *J* = 7.2 Hz, 2H), 7.75 (t, *J* = 7.5 Hz, 1H), 7.60−7.54 (m, 4H) ppm. $^{13}$C NMR (126 MHz, DMSO-$d_6$) δ: 158.62, 158.54, 154.90, 154.81, 154.45, 153.80, 153.72, 143.62, 143.03, 142.95, 135.14, 132.39, 130.03, 129.97, 128.89, 127.80, 127.61, 127.20, 124.04 ppm. HRMS: $C_{36}H_{26}IrN_6^{3+}$ Calcd: 245.0617, Found: 245.0623; $C_{36}H_{25}IrN_6^{2+}$ Calcd: 367.0886, Found: 367.0884.

*1T-Ir.* Compounds (**Ph-tpy**)$IrCl_3$ (231 mg, 0.381 mmol), **1T-tpy** (120 mg, 0.381 mmol), and ethylene glycol (17.0 mL) were used. The product obtained was a yellow powder (260 mg, yield: 74%). $^1$H NMR (500 MHz, DMSO-$d_6$): δ 9.68 (s, 2H), 9.53 (s, 2H), 9.36 (d, *J* = 6.3 Hz, 2H), 9.32 (d, *J* = 7.9 Hz, 2H), 8.72 (s, br., 1H), 8.52 (d, *J* = 7.5 Hz, 2H), 8.38−8.34 (m, 4H), 8.17 (d, *J* = 5.0 Hz, 1H), 8.03 (d, *J* = 5.6 Hz, 2H), 7.97 (d, *J* = 5.6 Hz, 2H), 7.83 (t, *J* = 7.5 Hz, 2H), 7.75 (t, *J* = 7.3 Hz, 1H), 7.58 (t, *J* = 6.7 Hz, 3H), 7.55 (t, *J* = 5.0 Hz, 2H) ppm. $^{13}$C NMR (126 MHz, DMSO-$d_6$) δ 158.72, 158.56, 154.99, 154.90, 154.39, 153.83, 153.73, 148.25, 142.95, 142.90, 139.13, 135.16, 133.89, 132.37, 132.19, 130.19, 130.03, 130.00, 129.97, 128.90, 127.92, 127.81, 124.04, 122.01 ppm. HRMS: $C_{40}H_{28}IrN_6S^{3+}$ Calcd: 272.3909, found: 272.3915; $C_{40}H_{27}IrN_6S^{2+}$ Calcd: 408.0824, found: 408.0824.

*2T-Ir.* Compounds (**Ph-tpy**)$IrCl_3$ (138 mg, 0.227 mmol), **2T-tpy** (90.0 mg, 0.227 mmol), and ethylene glycol (10.0 mL) were used. The final product was obtained as a light orange powder (160 mg, yield: 70%). $^1$H NMR (500 MHz, DMSO-$d_6$): δ 9.66 (s, 2H), 9.49 (s, 2H), 9.28 (t, *J* = 9.1 Hz, 4H), 8.66 (d, *J* = 4.0 Hz, 1H), 8.49 (d, *J* = 7.6 Hz, 2H), 8.38 (tt, *J* = 7.9, 1.9 Hz, 4H), 8.03 (dd, *J* = 5.8, 1.4 Hz, 2H), 7.96 (dd, *J* = 5.8, 1.4 Hz, 2H), 7.87−7.82 (m, 3H), 7.78−7.74 (m,


https://doi.org/10.1021/acs.inorgchem.4c03847
Inorg. Chem. 2024, 63, 21323−21335

2H), 7.65 (dd, $J$ = 3.6, 1.2 Hz, 1H), 7.61−7.55 (m, 4H), 7.28 (dd, $J$ = 5.1, 3.6 Hz, 1H) ppm. $^{13}$C NMR (126 MHz, DMSO-$d_6$) $\delta$: 158.72, 158.57, 155.00, 154.82, 153.74, 147.56, 143.51, 142.90, 137.11, 135.77, 135.17, 133.62, 130.04, 129.98, 129.49, 128.88, 128.41, 127.78, 126.66, 124.02, 121.53 ppm. HRMS: $C_{44}H_{30}IrN_6S_2^{3+}$ Calcd: 299.7201, found: 299.7206; $C_{44}H_{29}IrN_6S_2^{2+}$ Calcd: 449.0762, found: 449.0762.

*3T-Ir*. Compounds **(Ph-tpy)IrCl$_3$** (121 mg, 0.199 mmol), **3T-tpy** (96 mg, 0.199 mmol), and ethylene glycol (10.0 mL) were used. The product obtained was a dark red powder (80 mg, yield: 35%). $^1$H NMR (500 MHz, DMSO-$d_6$): $\delta$ 9.67 (s, 2H), 9.51 (s, 2H), 9.32 (d, $J$ = 7.9 Hz, 2H), 9.29 (d, $J$ = 8.0 Hz, 2H), 8.71 (d, $J$ = 4.0 Hz, 1H), 8.50 (d, $J$ = 7.3 Hz, 2H), 8.38 (tt, $J$ = 7.9, 1.4 Hz, 4H), 8.04 (dd, $J$ = 5.8, 1.4 Hz, 2H), 7.97 (dd, $J$ = 5.6, 1.5 Hz, 2H), 7.87 (d, $J$ = 3.9 Hz, 1H), 7.84 (t, $J$ = 5.4 Hz, 2H), 7.76 (tt, $J$ = 7.4, 1.3 Hz, 1H), 7.65 (dd, $J$ = 5.1, 1.1 Hz, 1H), 7.62 (d, $J$ = 3.8 Hz, 1H), 7.60−7.56 (m, 4H), 7.49−7.46 (m, 2H), 7.19 (dd, $J$ = 5.1, 3.6 Hz, 1H) ppm. $^{13}$C NMR (126 MHz, DMSO-$d_6$) $\delta$ 158.68, 158.53, 154.97, 154.79, 154.46, 153.81, 153.70, 147.43, 142.98, 142.92, 142.87, 138.20, 137.27, 135.96, 135.20, 134.19, 133.65, 132.37, 130.05, 130.00, 129.20, 128.87, 127.79, 127.12, 126.79, 125.96, 125.60, 124.04, 121.52 ppm. HRMS: $C_{48}H_{32}IrN_6S_3^{3+}$ Calcd: 327.0493, Found: 327.0499; $C_{48}H_{31}IrN_6S_3^{2+}$ Calcd: 490.0700, found: 490.0698.

*4T-Ir*. Compounds **(Ph-tpy)IrCl$_3$** (61.0 mg, 0.100 mmol), **4T-tpy** (56 mg, 0.100 mmol), and ethylene glycol (5.0 mL) were used. The product obtained was a dark red powder (16 mg, yield: 13%). $^1$H NMR (500 MHz, DMSO-$d_6$): $\delta$ 9.69 (s, 2H), 9.56 (s, 2H), 9.37 (dd, $J$ = 8.1, 1.4 Hz, 2H), 9.33 (dd, $J$ = 8.0, 1.5 Hz, 2H), 8.78 (d, $J$ = 4.1 Hz, 1H), 8.53 (d, $J$ = 7.4 Hz, 2H), 8.38 (tt, $J$ = 7.8, 1.5 Hz, 4H), 8.05 (dd, $J$ = 5.7, 1.4 Hz, 2H), 7.98 (dd, $J$ = 5.7, 1.4 Hz, 2H), 7.86 (d, $J$ = 3.8 Hz, 1H), 7.83 (t, $J$ = 7.5 Hz, 2H), 7.76 (t, $J$ = 7.3 Hz, 1H), 7.64 (d, $J$ = 3.8 Hz, 1H), 7.62−7.55 (m, 5H), 7.52 (d, $J$ = 3.8 Hz, 1H), 7.45 (d, $J$ = 3.7 Hz, 1H), 7.42 (dd, $J$ = 3.5, 1.2 Hz, 1H), 7.38 (d, $J$ = 3.8 Hz, 1H), 7.16 (dd, $J$ = 5.1, 3.6 Hz, 1H). $^{13}$C NMR (126 MHz, DMSO-$d_6$) $\delta$: 158.72, 158.58, 154.99, 154.81, 154.41, 153.84, 153.73, 147.42, 142.96, 142.90, 142.71, 137.54, 137.44, 136.95, 136.17, 135.17, 134.60, 134.46, 133.89, 132.36, 130.02, 129.99, 129.07, 128.92, 127.91, 127.84, 126.94, 126.70, 126.58, 126.21, 125.71, 125.21, 124.06, 121.62 ppm. HRMS: $C_{52}H_{34}IrN_6S_4^{3+}$ Calcd: 354.3785, Found: 354.3782; $C_{52}H_{33}IrN_6S_4^{2+}$ Calcd: 531.0638, found: 531.0630.

**Photophysical Studies.** The UV−vis absorption spectra of the Cl$^-$ salts of **0T-Ir**−**4T-Ir** were measured in dilute methanol solutions (5−20 $\mu$M) on a Jasco v730 dual beam spectrophotometer. Steady-state emission spectra were measured on a PTI Quantamaster spectrometer with a K170B PMT detector for visible and NIR emission (max ≈ 800 nm), and a Hamamatsu R5509−42 PMT (600−1400 nm) for longer wavelength emission measurements. Each sample was excited at its most intense and longest-wavelength peak. Degassed dilute methanol solution of each complex was used for the room temperature emission study. Five free-pump-thaw cycles in a custom Schlenk-style cuvette were performed to completely remove air from the sample solutions. Emission at 77 K was measured in a 4/1 (v/v) EtOH/MeOH glassy matrix in a 5 mm NMR tube immersed in liquid nitrogen in a custom apparatus.

The differential triplet transient absorption (TA) spectra and the triplet decay characteristics were investigated on an Edinburgh LP-980 laser flash photolysis spectrometer with a PMT-LP detector. The methanol solution of each sample was degassed by five freeze−pump−thaw cycles prior to measurement. The pump beam was provided by a Continuum Minilite Nd:YAG laser at 355 nm (the pulse width is approximately 5 ns and the energy per pulse is ca. 7−9 mJ). The sample concentration was adjusted to reach an absorbance of ca. 0.4 in a 1 cm cuvette at 355 nm. The triplet lifetimes were deduced from the decay curves of the transient signals at the corresponding wavelengths of the TA band maxima.

**Singlet Oxygen Quantum Yield Measurements.** The singlet oxygen generation ($^1O_2$) was studied in air-saturated acetonitrile solutions of each sample by monitoring the $^1O_2$ emission band near 1268 nm. The $^1O_2$ quantum yield ($\Phi_\Delta$) was calculated by actometry using Ru(bpy)$_3$(PF$_6$)$_2$ in aerated acetonitrile as the reference ($\Phi_\Delta$ = 0.56).[43] The $^1O_2$ emission signal was measured on a PTI Quantamaster emission spectrometer with a 1000 nm long pass filter and a Hamamatsu R5509−42 near-infrared PMT that was cooled to −80 °C.

**Computational Methodology.** Calculations of the UV−vis absorption spectra were carried out using Gaussian-16 software[44] at the density functional theory (DFT) level for the ground-state properties and time-dependent DFT (TDDFT) level for the singlet excited state properties.[45,46] The LANL2DZ basis set[47] was used for Ir(III) and the 6-31G* basis[48] was used for H, C, N, and S atoms of the complexes. Calculations were carried out using PBE0 functional.[49,50] For all calculations, the conductor polarizable continuum model (CPCM)[51] was utilized to simulate a methanol solvent environment. All TDDFT calculations were performed for the first 100 states, with each state being convolved by a Gaussian function with a 0.1 eV line width. This convolution mimics the vibrational broadening observed in the experimental absorption spectra. The calculated spectra were uniformly shifted by 0.2607 eV to aid in comparison with the experimental spectra. This shift constant was derived as an average from the individual shifts observed between the calculated and experimental absorption spectra for each Ir(III) complex. Additionally, natural transition orbitals (NTOs)[52] were generated from the transition density matrix obtained from the TDDFT calculations and then visualized using the isovalue of 0.02 to provide insight into the nature of the electron−hole pairs contributing to the main absorption bands.

The emission spectra were calculated based on the optimization of the first singlet excited state using the analytical gradient time-dependent DFT (AG-TDDFT) with implemented spin−orbit couplings (SOCs), as provided in the ORCA 5.04 software package.[53] The trial wave function for optimizing the first excited state was derived from the geometry obtained during ground state optimization as described above using Gaussian 16 software.[44] The AG-TDDFT/SOC calculations utilized the PBE0 hybrid functional and the mixed basis set containing ZORA-def2-TZVP[54] for C, H, N, and S atoms, and SARC-ZORA-def2-TZVP[54] for Ir(III), with SARC/J auxiliary basis set being used in addition for all atoms. Methanol solvent was included in all calculations using the CPCM model.[51] Optical transitions obtained from AG-TDDFT/SOC calculations were convolved by a Gaussian function with a 0.2 eV line width in order to mimic the vibrational broadening observed in the experimental emission spectra. The isovalue of 0.02 was used to visualize molecular orbitals (MOs) that contribute to the electron−hole pairs responsible for the main emission states.

**Photobiological Studies.** The *in vitro* cytotoxicity and photocytotoxicity of the complexes against normoxic and hypoxic melanoma cells (SKMEL28, A375, and B16F10) and breast cancer cells (MDA-MB-231 and MCF-7) were evaluated according to our published procedures.[36] Dose−response curves were fitted using a nonlinear-regression sigmoidal dose−response curve model (GraphPad software, Inc., San Diego, USA) to yield EC$_{50}$ values calculated as the average of three independent replicates with variation reported as the standard deviation of the mean.[55] One-way ANOVA analysis with Tukey's test as post-ANOVA analysis ($p$ < 0.05) was used to test for statistical significance. The details regarding the use of scavengers and probes for identifying the RMS that may be implicated in photocytotoxicity are provided in the Supporting Information.

## RESULTS AND DISCUSSION

**Synthesis and Characterization.** The ligands were prepared following literature procedures, as shown in Scheme 1. The precursor **(Ph-tpy)IrCl$_3$** and ***n*T-tpy** were then reacted to form the desired products ***n*T-Ir** ($n$ = 0−4) alongside [(Ph-tpy)$_2$Ir]$^{3+}$, which were difficult to separate by manual column chromatography and required a CombiFlash Chromatograph System to obtain the desired Cl$^-$ salt of the product with >95% purity via HPLC analysis. The proton NMR signals were assigned by analyzing the chemical shifts and splitting patterns


https://doi.org/10.1021/acs.inorgchem.4c03847
Inorg. Chem. 2024, 63, 21323−21335

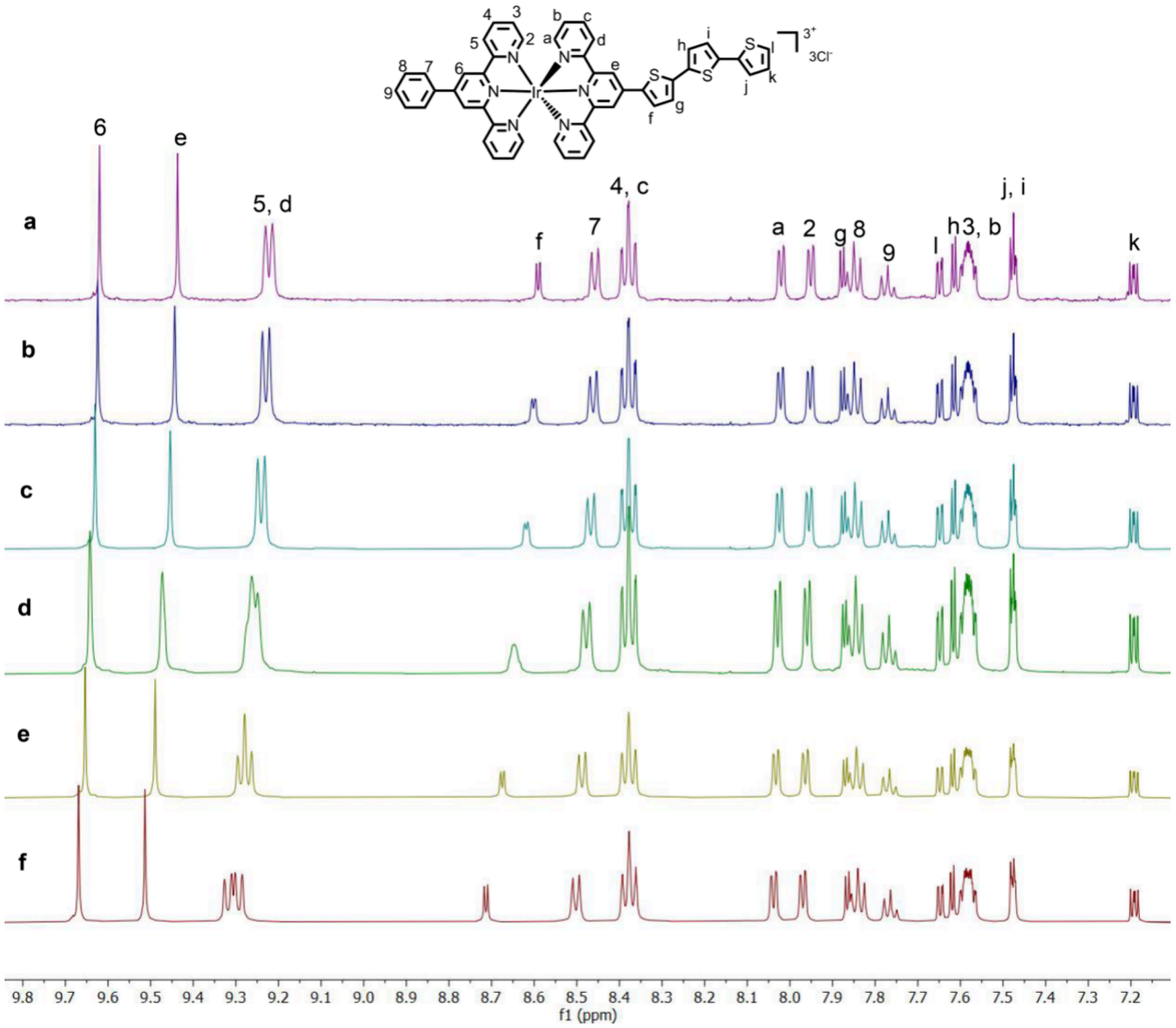


**Figure 1.** $^{1}$H NMR spectra of **3T-Ir** in DMSO-$d_6$. The concentrations of solutions are $6.47 \times 10^{-5}$, $1.29 \times 10^{-4}$, $2.59 \times 10^{-4}$, $5.18 \times 10^{-4}$, $1.04 \times 10^{-3}$, and $2.07 \times 10^{-3}$ mol/L for spectra of a–f, respectively.

and the correlations from the $^{1}$H–$^{1}$H COSY spectra. Formation of the desired products was further confirmed by high-resolution mass spectrometry. The 1D and 2D NMR spectra with proton assignments, the structures of the complexes with hydrogens labeled, the mass spectra, and the HPLC traces are provided in the Supporting Information (Figures S1–S22).

It is worth noting that the chemical shifts of protons 5, 6, and 7 on Ph-tpy and d, e, and f on ***n*T-tpy** ($n$ = 1–4, see labeling in Figure 1 and Supporting Information Figures S6 and S7), especially the $\beta$-proton on the thienyl ring directed attached to the tpy ligand (i.e., proton f), are impacted by the concentration of the solutions. As exemplified by the $^{1}$H NMR spectra of **3T-Ir** at different concentrations (Figure 1), the aforementioned NMR peaks progressively shifted downfield with an increasing concentration. This change may reflect the changes of dihedral angles between the phenyl/thienyl substituents and the tpy ligands due to increased intermolecular interactions and possible aggregation at higher concentration.

The complexes were stable in the dark but underwent some degree of photobleaching upon prolonged irradiation. As illustrated in Supporting Information Figure S23, the UV–vis absorption spectra of **2T-Ir** – **4T-Ir** in $H_2O$/DMSO (9/1, v/v) did not change over a 70 min observation window in the dark. However, the absorptivity of these solutions gradually decreased with broadband cool white light (400–700 nm) irradiation.

**UV–vis Absorption.** The UV–vis absorption spectra of the $Cl^-$ salts of **0T-Ir** – **4T-Ir** were measured in methanol solutions in a concentration range of 5–20 $\mu$M. The absorption followed Beer's law in the concentration range investigated and the absorption spectra are provided in Figure 2. The absorption band maxima and molar extinction coefficients are listed in Table 1. All complexes exhibited structured absorption bands below 365 nm with large molar extinction coefficients, which can be ascribed to the tpy-ligand-localized $^{1}\pi,\pi^*$ transitions. Except for **0T-Ir**, the other four complexes with 1–4 (oligo)thienyl substituents exhibited a broad, featureless absorption band at >365 nm. This band gradually red shifts when the number of thienyl groups


https://doi.org/10.1021/acs.inorgchem.4c03847
Inorg. Chem. 2024, 63, 21323–21335

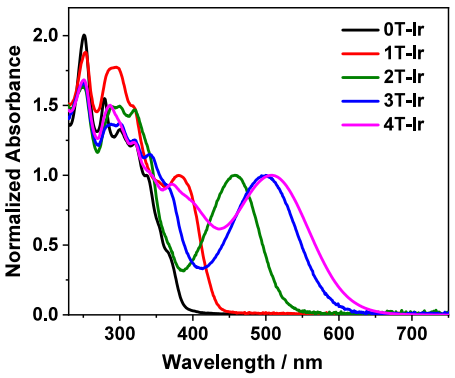


**Figure 2.** Normalized UV−vis absorption spectra of **0T-Ir**−**4T-Ir** in methanol. **0T-Ir** is normalized to the absorption band at 337 nm, and **1T-Ir**−**4T-Ir** is normalized to their corresponding low-energy absorption bands.

increases. Based on the shape of this band, the moderate to strong molar extinction coefficients, and the dependence on the number of thienyl groups, this band is mainly attributed to the ***n*T-tpy** ($n$ = 1−4)-based transitions including the $^1\pi,\pi^*$ transitions within the $n$T-pyridine component and the intraligand charge transfer ($^1$ILCT) from the oligothiophene to tpy ligand, possibly mixed with metal-to-ligand charge transfer ($^1$MLCT), ligand-to-metal charge transfer ($^1$LMCT), and ligand-to-ligand charge transfer ($^1$LLCT) from the ***n*T-tpy** ligand to the **Ph-tpy** ligand. This assignment is supported by the TDDFT calculations (Supporting Information Figures S24 and S25), as demonstrated by the NTOs shown in Table 2 for the $S_1$−$S_3$ states of **0T-Ir** − **4T-Ir** and in Supporting Information Table S2 for the high-energy excited states. The NTOs in Table 2 clearly show that the involvement of the $d$ orbitals in the holes of $S_1$ and $S_2$ states diminishes when the number of thienyl groups increases, which decreases the contribution of $^1$MLCT transitions to the low-energy absorption bands on going from **0T-Ir** to **4T-Ir**. Especially in **3T-Ir** and **4T-Ir**, the ***n*T-tpy** ligand localized $^1\pi,\pi^*$/$^1$ILCT transitions become the dominant contributors, admixing with some $^1$LMCT transitions. Probably due to the different degrees of contributions from the $^1\pi,\pi^*$, $^1$ILCT, $^1$MLCT, $^1$LMCT, and $^1$LLCT transitions, the molar extinction coefficients of this low-energy absorption band do not follow a systematic trend.

The minor solvatochromic effects observed from these complexes (Supporting Information, Figure S26) also support the mixed nature of the electronic configurations giving rise to these absorption bands.

Another possible attribution to this nonmonotonic trend could be the agglomeration effect in methanol solutions although no visible aggregates were observed in these solutions, which would change the torsional angles between the tpy ligand and the thienyl group directly attached to it. Our TDDFT calculations show that variations of this angle drastically change the shape and intensity of this absorption band (Supporting Information Figure S27). The piece of experimental evidence that could support the agglomeration effect comes from the UV−vis absorption study of **4T-Ir** in mixed DMSO/$H_2O$ solutions with varied percentage of $H_2O$ content ($H_2O$ is a poor solvent for these complexes). As presented in Supporting Information Figure S28, the increased $H_2O$ content in solutions gradually reduced the absorptivity of the solutions and caused a minor red-shift of the low-energy absorption band and a slight blue-shift of the high-energy absorption band.

**Photoluminescence.** The emission of **0T-Ir**−**4T-Ir** was studied in methanol solutions at room temperature (rt) and in 4/1 (v/v) EtOH/MeOH glassy matrix at 77 K. Upon excitation at their corresponding lowest-energy absorption bands, all complexes are weakly emissive at rt in methanol. As shown in Figure 3, the spectrum of **0T-Ir** exhibited a vibronic structure, possibly originating from the **Ph-tpy** ligand-localized $^3\pi,\pi^*$ excited state. For **1T-Ir** and **2T-Ir**, the significantly red-shifted emission is tentatively ascribed to ***n*T-tpy** ligand-localized $^3$ILCT/$^3\pi,\pi^*$ excited states admixing with $^3$MLCT configurations as we reported for related $[Ir(Ar\text{-}tpy)(Ph\text{-}tpy)]^{3+}$ complexes previously.[29] Both **3T-Ir** and **4T-Ir** exhibited dual emission, with the shorter wavelength band being ascribed to ***n*T-tpy** ligand-localized $^1\pi,\pi^*$/$^1$ILCT fluorescence and the longer wavelength shoulder being ascribed to $^3\pi,\pi^*$/$^3$ILCT states. Ligand-localized $^1\pi,\pi^*$/$^1$ILCT ***n*T-tpy** fluorescence was assigned based on a comparison with the corresponding free ***n*T-tpy** ligands, which do not phosphoresce (Supporting Information Figure S29) while the assignment of the longer wavelength bands was made based on our previously reported Ir(III) and Ru(II) bis-tpy complexes bearing $\pi$-expansive Ar-tpy ligands.[29,33] The blue-

**Table 1. Photophysical Parameters of 0T-Ir−4T-Ir**

| | $\lambda_{abs}$/nm ($\varepsilon$ /L·mol$^{-1}$·cm$^{-1}$)[a] | $\lambda_{em}$/nm[b] R.T. | $\lambda_{em}$/nm[b] 77 K | $\lambda_{T1-Tn}$/nm[c] ($\tau_T$/$\mu$s) | $\Phi_\Delta$ ($\lambda_{ex}$/nm)[d] |
|---|---|---|---|---|---|
| **0T-Ir** | 251 (46040), 279 (35600), 301 (30520), 321 (28220), 337 (22970), 365 (10440) | 494, 520 | 476, 507, 535, 577 (sh.), 630 (sh.) | 380 (0.29), 630 (0.31) | 0.04 (322) |
| **1T-Ir** | 253 (41960), 295 (39590), 318 (33410), 381 (22300) | 558, 582 (sh.) | 537, 581, 630, 688 (sh.) | 620 (0.57) | 0.20 (384) |
| **2T-Ir** | 251 (23840), 290 (21730), 300 (21780), 321 (21390), 457 (14560) | 720, 763 (sh.) | 511, 679, 749, 829, 930 (sh.) | 725 (35) | 0.84 (460) |
| **3T-Ir** | 250 (40950), 288 (33530), 299 (33660), 320 (30750), 341 (28210), 500 (24520) | 658, 794 | 579, 623 (sh.) | 565 (5.8), 720 (−) | 0.64 (476) |
| **4T-Ir** | 251 (27210), 287 (24270), 320 (19970), 370 (15130), 508 (16160) | 601, 822 | 609, 639 (sh.) | 650 (0.30 (73%), 2.0 (27%)) | 0.34 (472) |

[a]Absorption band maxima ($\lambda_{abs}$) and molar extinction coefficients ($\varepsilon$) at room temperature in methanol. [b]Emission band maxima ($\lambda_{em}$) at room temperature and 77 K, $\lambda_{ex}$ = 366, 379, 454, 494, and 508 nm for **0T-Ir**−**4T-Ir**, respectively. The emission lifetimes were too short, or the signals were too weak to allow for the lifetimes to be measured. [c]Nanosecond TA band maxima ($\lambda_{T1-Tn}$) and triplet excited−state lifetimes ($\tau_T$) were measured at room temperature in deaerated $CH_3CN$. [d]Singlet oxygen generation efficiency ($\Phi_\Delta$) in aerated $CH_3CN$ at the indicated excitation wavelengths. $Ru(bpy)_3(PF_6)_2$ in aerated $CH_3CN$ was used as the reference ($\Phi_\Delta$ = 0.56).[43]



https://doi.org/10.1021/acs.inorgchem.4c03847
Inorg. Chem. 2024, 63, 21323−21335

**Table 2. NTOs of the Transitions Contributing to the Low-energy Absorption Band, Calculated Using the TDDFT Method with the PBE0 Functional and LANL2dz/6-31G* Basis Set in Methanol**

| | Excited States and Properties[a] | Hole | Electron | Predominant Characters |
|---|---|---|---|---|
| **0T-Ir** | $S_1$ 328 nm *f=0.4181* | 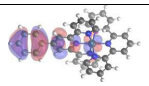 | 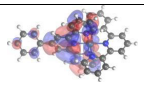 | $^1\pi,\pi^*/^1$ILCT /$^1$MLCT/$^1$LMCT |
| | $S_2$ 320 nm *f=0.0002* | 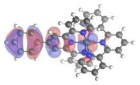 | 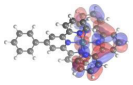 | $^1$LLCT/$^1$MLCT /$^1$LMCT |
| | $S_3$ 319 nm *f=0.0243* | 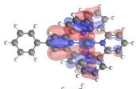 | 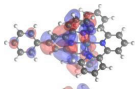 | $^1\pi,\pi^*/^1$MLCT /$^1$LMCT |
| **1T-Ir** | $S_1$ 358 nm *f=0.6902* | 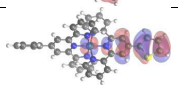 | 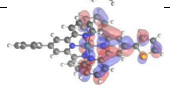 | $^1\pi,\pi^*/^1$ILCT /$^1$MLCT/$^1$LMCT |
| | $S_2$ 351 nm *f=0.0000* | 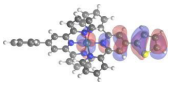 | 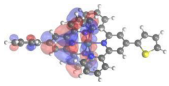 | $^1$LLCT/$^1$MLCT /$^1$LMCT |
| | $S_3$ 340 nm *f=0.0020* | 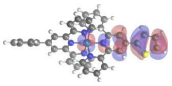 | 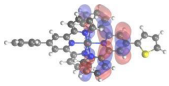 | $^1$ILCT/$^1$MLCT /$^1\pi,\pi^*$ |
| **2T-Ir** | $S_1$ 454 nm *f=0.9010* | 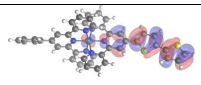 | 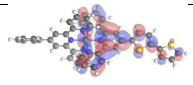 | $^1\pi,\pi^*/^1$ILCT /$^1$MLCT/$^1$LMCT |
| | $S_2$ 436 nm *f=0.0001* | 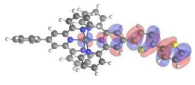 | 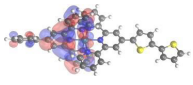 | $^1$LLCT/$^1$MLCT /$^1$LMCT |
| | $S_3$ 412 nm *f=0.0116* | 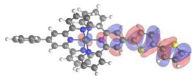 | 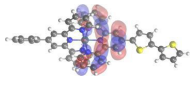 | $^1$ILCT/$^1$MLCT /$^1\pi,\pi^*$ |
| **3T-Ir** | $S_1$ 527 nm *f=1.0837* | 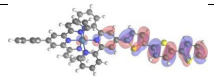 | 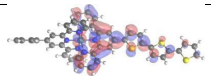 | $^1\pi,\pi^*/^1$ILCT /$^1$LMCT/$^1$MLCT |
| | $S_2$ 499 nm *f=0.0001* | 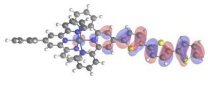 | 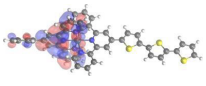 | $^1$LLCT/$^1$LMCT /$^1$MLCT |
| | $S_3$ 459 nm *f=0.0170* | 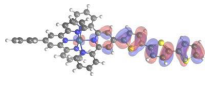 | 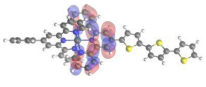 | $^1$ILCT/$^1$MLCT /$^1\pi,\pi^*$ |
| **4T-Ir** | $S_1$ 578 nm *f=1.1223* | 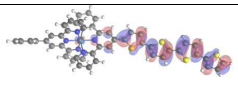 | 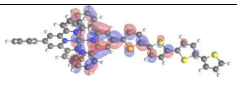 | $^1\pi,\pi^*/^1$ILCT /$^1$LMCT/$^1$MLCT |
| | $S_2$ 542 nm *f=0.0001* | 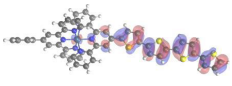 | 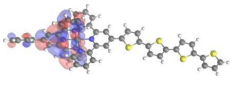 | $^1$LLCT/$^1$LMCT /$^1$MLCT |
| | $S_3$ 489 nm *f=0.0186* | 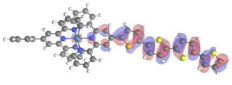 | 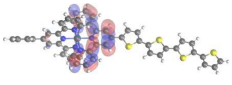 | $^1$ILCT/$^1$MLCT /$^1\pi,\pi^*$ |

shifted emission at 77 K for **0T-Ir** - **2T-Ir** exhibited vibronic structures and the thermochromic shifts were in the range of 666−839 $cm^{-1}$, implying that their emitting states have a significant $^3\pi,\pi^*$ character. In contrast, the 77 K emission profiles for **3T-Ir** and **4T-Ir** were dominated by the shorter wavelength fluorescence and showed a less vibronic structure.

Assignment of the emitting states is supported by AG-TDDFT calculations. As shown in Supporting Information Figure S30 and Table S3, the emitting triplet excited states for all complexes admix $^3\pi,\pi^*/^3$ILCT/$^3$MLCT/$^3$LMCT characters. However, when the number of the thienyl ring increases, contribution from the $^3$MLCT/$^3$LMCT transitions diminishes and $^3\pi,\pi^*/^3$ILCT transitions emerge as the dominant configuration. This characteristic becomes more salient in **3T-Ir** and **4T-Ir**. Similar to the emitting triplet excited states, the emitting singlet excited states possess the mixed $^1\pi,\pi^*/^1$ILCT/$^1$MLCT/$^1$LMCT configurations, with $^1\pi,\pi^*/^1$ILCT being the dominant configurations in **3T-Ir** and **4T-Ir**.

**Triplet Transient Absorption (TA).** The triplet transient difference absorption spectra of **0T-Ir** − **4T-Ir** were studied in deaerated $CH_3CN$ solutions. The time-resolved transient



https://doi.org/10.1021/acs.inorgchem.4c03847
Inorg. Chem. 2024, 63, 21323−21335

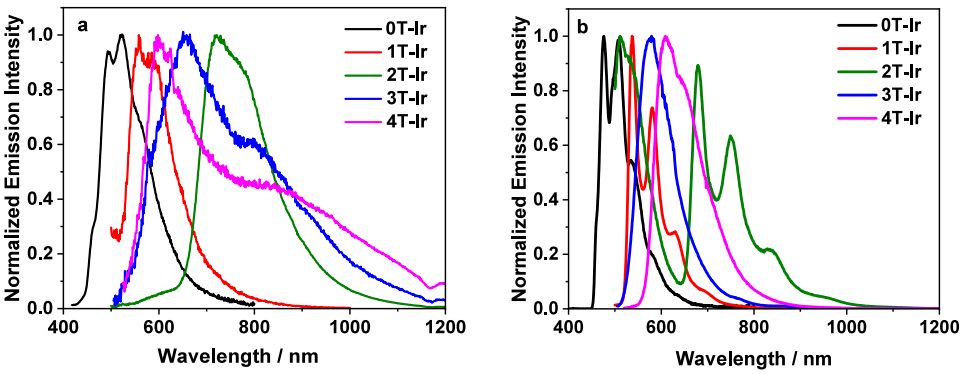


**Figure 3.** Normalized emission spectra of **0T-Ir**–**4T-Ir** (a) in methanol at room temperature and (b) in an EtOH/MeOH (4/1, v/v) glassy matrix at 77 K.

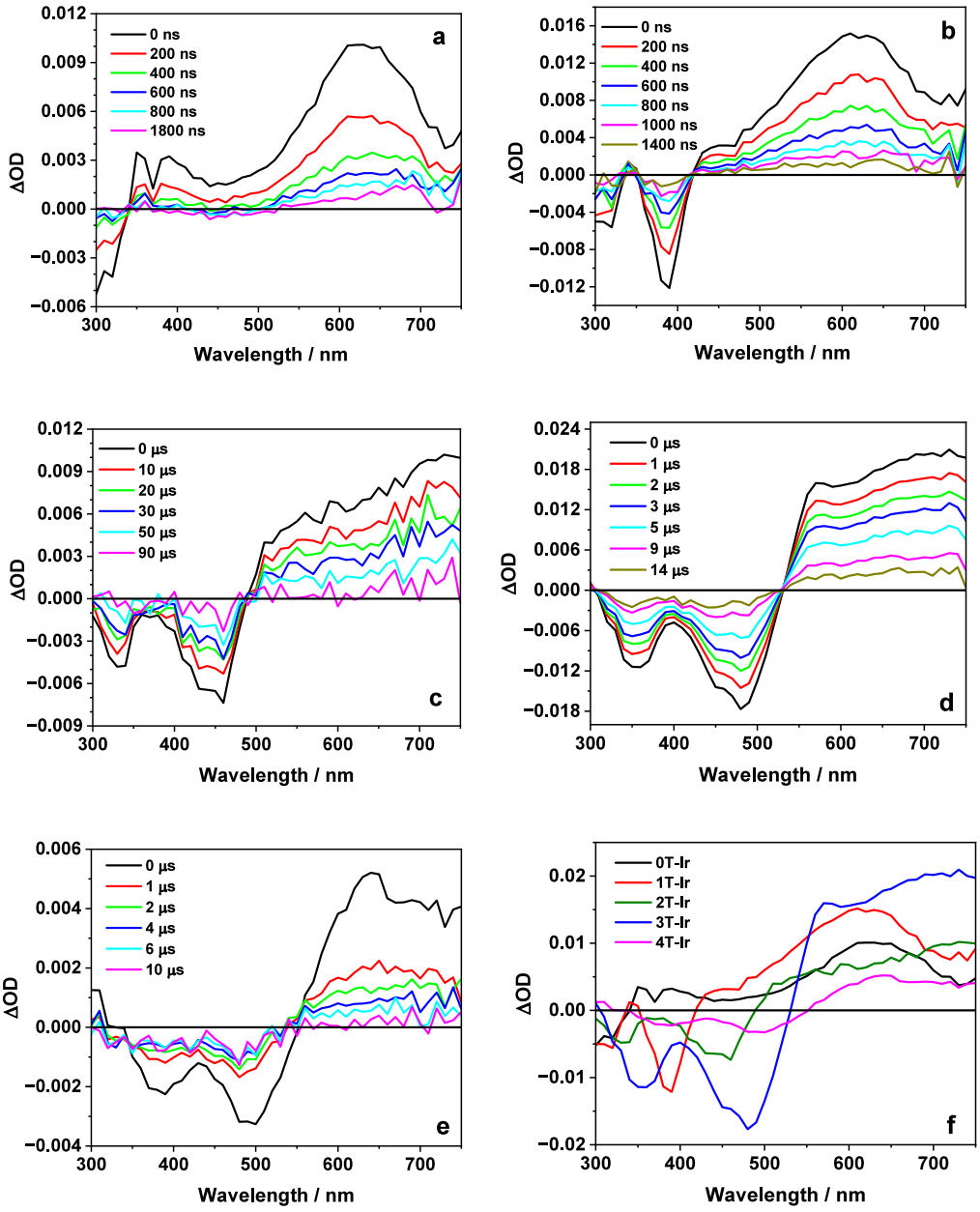


**Figure 4.** Time-resolved transient differential absorption spectra of **0T-Ir**–**4T-Ir** in deaerated acetonitrile solutions ($A_{355\ nm}$ = 0.4) in a 1 cm cuvette: (a) **0T-Ir**, (b) **1T-Ir**, (c) **2T-Ir**, (d) **3T-Ir**, (e) **4T-Ir**, and (f) stacked spectra of ***n*T-Ir** at zero delay after excitation.



https://doi.org/10.1021/acs.inorgchem.4c03847
*Inorg. Chem.* 2024, 63, 21323−21335

Table 3. Cytotoxicity and Photocytotoxicity ($EC_{50}$ Values/$\mu$M) of *n*T-Ir on SKMEL28, A375, and B16F10 Cells under Normoxic (~18.5% $O_2$) and Hypoxic (1% $O_2$) Conditions[a,b]

| | | | | | | | | PI[c] | | | |
|---|---|---|---|---|---|---|---|---|---|---|---|
| cell line | complex | $O_2$ (%) | dark | visible[d] | blue[e] | green[f] | red[g] | visible[d] | blue[e] | green[f] | red[g] |
| SKMEL28 | 0T-Ir | ~18.5 | >300 | 180 ± 11 | 263 ± 22 | >300 | >300 | ~2 | ~1 | ~1 | ~1 |
| | | 1 | >300 | >300 | >300 | >300 | >300 | ~1 | ~1 | ~1 | ~1 |
| | 1T-Ir | ~18.5 | >300 | 38.7 ± n.d. | 41.5 ± n.d. | 181 ± 4 | >300 | ~8 | ~7 | ~2 | ~1 |
| | | 1 | >300 | >300 | >300 | >300 | >300 | ~1 | ~1 | ~1 | ~1 |
| | 2T-Ir | ~18.5 | >300 | 0.313 ± 0.021 | 0.334 ± 0.006 | 0.574 ± 0.051 | >300 | ~958 | ~898 | ~523 | ~1 |
| | | 1 | >300 | >300 | >300 | >300 | >300 | ~1 | ~1 | ~1 | ~1 |
| | 3T-Ir | ~18.5 | 59.8 ± 1.2 | 0.0942 ± n.d. | 0.142 ± n.d. | 0.160 ± n.d. | 4.32 ± 0.09 | 635 | 421 | 374 | 14 |
| | | 1 | 61.2 ± 1.2 | 5.48 ± n.d. | 5.44 ± n.d. | 5.33 ± n.d. | 63.2 ± 1.5 | 11 | 11 | 11 | 1 |
| | 4T-Ir | ~18.5 | 86.0 ± 2.7 | 0.327 ± 0.050 | 0.646 ± n.d. | 0.292 ± 0.032 | 3.19 ± 0.74 | 263 | 133 | 295 | 27 |
| | | 1 | 89.2 ± 2.5 | 4.95 ± n.d. | 4.98 ± n.d. | 2.96 ± 0.25 | 85.3 ± 2.1 | 18 | 18 | 30 | 1 |
| A375 | 0T-Ir | ~18.5 | 81.2 ± 9.8 | 28.7 ± 2.1 | 30.4 ± 1.9 | 61.9 ± 3.0 | 74.3 ± 7.4 | 3 | 3 | 1 | 1 |
| | | 1 | 127 ± 15 | 224 ± 28 | 191 ± 25 | 123 ± 14 | 118 ± 13 | 1 | 1 | 1 | 1 |
| | 1T-Ir | ~18.5 | >300 | 17.3 ± 0.1 | 18.3 ± 1.5 | >300 | >300 | ~17 | ~16 | ~1 | ~1 |
| | | 1 | >300 | >300 | >300 | >300 | >300 | ~1 | ~1 | ~1 | ~1 |
| | 2T-Ir | ~18.5 | >300 | 0.662 ± 0.071 | 0.811 ± 0.056 | 2.70 ± 0.34 | >300 | ~453 | ~370 | ~111 | ~1 |
| | | 1 | >300 | >300 | >300 | >300 | >300 | ~1 | ~1 | ~1 | ~1 |
| | 3T-Ir | ~18.5 | 28.7 ± 1.3 | 0.149 ± 0.008 | 0.211 ± 0.032 | 0.273 ± 0.031 | 3.33 ± 0.27 | 193 | 136 | 105 | 9 |
| | | 1 | 48.8 ± n.d. | 5.29 ± n.d. | 5.30 ± n.d. | 32.4 ± 5.5 | 30.2 ± 1.8 | 9 | 9 | 2 | 2 |
| | 4T-Ir | ~18.5 | 46.1 ± 1.4 | 0.0206 ± 0.0009 | 0.0355 ± 0.0039 | 0.0410 ± 0.0021 | 1.85 ± 0.11 | 2238 | 1299 | 1124 | 25 |
| | | 1 | 45.2 ± 1.2 | 0.788 ± 0.156 | 0.952 ± 0.217 | 0.546 ± 0.162 | 35.9 ± 2.2 | 57 | 47 | 83 | 1 |
| B16F10 | 0T-Ir | ~18.5 | >300 | 161 ± 7 | 184 ± 7 | >300 | >300 | ~2 | ~2 | ~1 | ~1 |
| | | 1 | >300 | >300 | >300 | >300 | >300 | ~1 | ~1 | ~1 | ~1 |
| | 1T-Ir | ~18.5 | >300 | 23.7 ± 1.4 | 26.6 ± 1.5 | >300 | >300 | ~13 | ~11 | ~1 | ~1 |
| | | 1 | >300 | >300 | >300 | >300 | >300 | ~1 | ~1 | ~1 | ~1 |
| | 2T-Ir | ~18.5 | >300 | 0.225 ± 0.013 | 0.373 ± 0.028 | 1.80 ± 0.11 | >300 | ~1333 | ~804 | ~167 | ~1 |
| | | 1 | >300 | >300 | >300 | >300 | >300 | ~1 | ~1 | ~1 | ~1 |
| | 3T-Ir | ~18.5 | 55.6 ± 4.2 | 0.0952 ± 0.0027 | 0.305 ± 0.018 | 0.446 ± 0.178 | 6.39 ± 0.09 | 584 | 182 | 125 | 9 |
| | | 1 | 53.6 ± 2.8 | 69.5 ± 3 | 67.1 ± 3.2 | 63.9 ± 3.2 | 58.7 ± 2.8 | 1 | 1 | 1 | 1 |
| | 4T-Ir | ~18.5 | 95.7 ± 3.1 | 0.0456 ± 0.0048 | 0.0736 ± 0.0046 | 0.131 ± 0.010 | 4.11 ± 0.14 | 2099 | 1300 | 731 | 23 |
| | | 1 | 94.6 ± 4.0 | 10.8 ± 1.9 | 13.2 ± 1.7 | 11.1 ± 1.1 | 89.7 ± 3.9 | 9 | 7 | 9 | 1 |

[a]Hypoxia and normoxia experiments were ran in parallel. [b]n.d. = SEM not determined due to steep hill slope. [c]PI = phototherapeutic index. [d]Cool white visible (400−700 nm). [e]Blue (453 nm). [f]Green (523 nm). [g]Red (633 nm). Light treatments were approximately 100 J $cm^{-2}$ delivered at 18−24 mW $cm^{-2}$.

difference absorption spectra of **0T-Ir**−**4T-Ir** are presented in Figure 4. The TA band maxima and triplet lifetimes measured at the band maxima are compiled in Table 1. **0T-Ir** exhibits broad positive absorption bands at 340−750 nm, with the maximum TA signal appearing at 625 nm. For **1T-Ir** − **4T-Ir**, the positive TA bands appear at 410−750, 490−750, 525−750, and 550−750 nm, respectively, while bleaching occurs at the corresponding $^1\pi,\pi^*/^1$CT (charge transfer) spectral regions. The triplet lifetimes increase from **0T-Ir** to **2T-Ir** and then decrease in **3T-Ir** and **4T-Ir**. This trend can be rationalized as the following: when the number of thienyl groups increases from **0T-Ir** to **2T-Ir**, the contribution of the ligand-localized $^3\pi,\pi^*$ configuration increases, resulting in an increased triplet lifetime. However, when the number of thienyl groups increases to 3 and 4, the triplet energy levels of the complexes are lowered, leading to increased nonradiative decays and reducing the triplet lifetime.

**Singlet Oxygen Generation.** Previously, we reported that Ir(R-tpy)(R′-tpy)$^{3+}$ (R = pyr, R′ = Ph; or R = R′ = pyr) complexes possessing long-lived triplet excited state exhibited high efficiency (ca. 80%) for generation of singlet oxygen.[29] Our TA study discussed above reveals that these *n*T-Ir complexes possess reasonably long-lived triplet excited states. Thus, they are expected to produce singlet oxygen in aerated solutions upon light activation. To demonstrate it, **0T-Ir**−**4T-Ir** were dissolved in acetonitrile solution and the singlet oxygen luminescence at 1268 nm was monitored. Acetonitrile was used as the solvent to avoid quenching of singlet oxygen phosphorescence by protic solvents. $Ru(bpy)_3(PF_6)_2$ was used as the reference for calculation of the singlet oxygen generation quantum yield ($\Phi_\Delta$). The obtained $\Phi_\Delta$ values for **0T-Ir**−**4T-Ir** are provided in Table 1, which follows the trend of increasing from **0T-Ir** to **2T-Ir** but decreasing from **2T-Ir** to **4T-Ir**. This trend parallels that of the triplet excited-state lifetimes in these complexes. Because singlet oxygen is produced via an energy transfer process from the triplet excited state of a PS to the ground-state oxygen, which is a bimolecular process. The longer the triplet excited-state lifetime of the PS, the more opportunity for it to encounter oxygen and thus the higher the singlet oxygen generation. This has been demonstrated by our group previously and holds the same in this series of complexes.[29]

***In Vitro* PDT.** Because of the ability of **0T-Ir**−**4T-Ir** to generate singlet oxygen upon visible light excitation, their potentials as PSs for PDT were assessed against three melanoma cell lines, i.e., SKMEL28, A375, and B16F10, and two breast cancer cell lines MDA-MB-231 and MCF-7 under nomoxia (~18.5% oxygen tension) and hypoxia (1% oxygen tension) upon broadband visible (400−700 nm), blue (453 nm), green (523 nm), and red (633 nm) light activation. The


https://doi.org/10.1021/acs.inorgchem.4c03847
Inorg. Chem. 2024, 63, 21323−21335

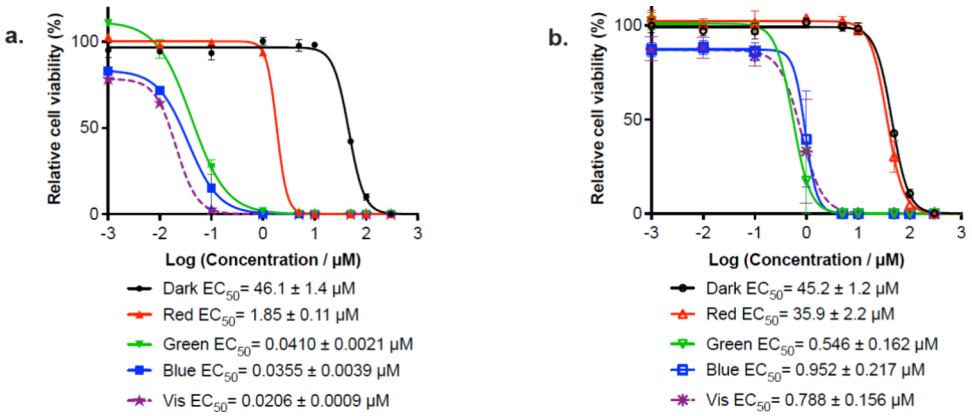


**Figure 5.** *In vitro* dose−response curves for **4T-Ir** toward A375 cells under (a) normoxia and (b) hypoxia without (black) or with broadband visible (400−700 nm, plum), blue (453 nm, blue), green (523 nm, green), or red (633 nm, red) light irradiation. Light treatments were approximately 100 J $cm^{-2}$ delivered at 18-24 mW $cm^{-2}$.

resultant $EC_{50}$ values and PI (phototherapeutic indices) values are provided in Table 3 and Supporting Information Tables S4 and S5, and the activity plots are exemplified in Figure 5 for **4T-Ir** toward A375 cells. A general trend observed is that **0T-Ir** - **2T-Ir** exhibited no dark cytotoxicity against all five cell lines without light activation, while **3T-Ir** and **4T-Ir** showed weak dark cytotoxicity. In contrast, upon broadband visible light and blue and green light activation, **2T-Ir**−**4T-Ir** exhibited strong photocytotoxicity toward all cell lines, giving submicromolar $EC_{50}$ values under normoxia. **3T-Ir** and **4T-Ir** also exhibited moderate PDT effects toward all cell lines upon red-light irradiation, with <10 $\mu$M $EC_{50}$ values and 7−27 PI margins. The strength of the PDT effect followed the trend of **2T-Ir** > **3T-Ir** ≥ **4T-Ir** toward SKMEL28, MDA-MB-231, and MCF-7 cells, which parallels the trend of singlet oxygen quantum yields of these three complexes; while for B16F10 and A375 cells, **4T-Ir** exhibited the strongest PDT effects (PI varied from 23 to 2238) followed by **2T-Ir** and then **3T-Ir** regardless of the excitation light wavelengths. Moreover, upon red-light excitation, **4T-Ir** showed the strongest PDT effects compared with the other four complexes toward all cell lines.

However, under hypoxia, the PDT effect was significantly attenuated regardless of the cell lines and excitation wavelengths. **3T-Ir** and **4T-Ir** gave $EC_{50}$ values of <70 $\mu$M and considerable PI margins (2−83) upon visible, blue, and green light activation toward the three melanoma cell lines, with **4T-Ir** showing 1 order of magnitude stronger PI values than those of **3T-Ir**. Especially **4T-Ir** gave a PI value of 83 toward the A375 cells with green light activation under hypoxia. To the best of our knowledge, this probably is the largest PI value for Ir(III)-based PSs upon green light activation under hypoxia. However, no complex showed PDT effects toward the two breast cancer cell lines under hypoxia.

Overall, **4T-Ir** was the top performer in terms of activity as defined by PI across all of the cancer cell lines and light conditions, and **0T-Ir** was the poorest. Both **1T-Ir** and **2T-Ir** were inactive in hypoxia under all of the conditions tested. Although **2T-Ir** stood out for its activity in normoxia, it surpassed only **4T-Ir** in one cell line. Blue and green light were most effective at activating the complexes and were the only wavelengths that resulted in activity in hypoxia for **4T-Ir**. The fact that photosensitizers such as **4T-Ir** are only active with red light under normoxia and would not be responsive to NIR light points toward their greatest utility, being applications where limited tissue penetration is desirable.

To gain a better understanding of which RMS could be involved in photocytotoxicity, we examined the effects of various probes (i.e., singlet oxygen sensor green (SOSG) as a fluorometric probe and anthracene-9,10-dipropionic acid disodium salt (ADPA) as the colorimetric probe for singlet oxygen, and hydroxyphenyl fluorescein (HPF) as the fluorometric probe for hydroxyl radicals and peroxynitrite anions) and scavengers (i.e., 1,4-diazabicyclo[2.2.2]octane (DABCO), $NaN_3$, and L-histidine for singlet oxygen, uric acid for peroxynitrite anions, mannitol, *tert*-butanol and DMSO for hydroxyl radicals, sodium pyruvate for hydrogen peroxide, and disodium 4,5-dihydroxy-1,3-benzenedisulfonate (Tiron) for superoxide anion radicals) on the cell-free and cellular responses (SKMEL28) of **0T-Ir** − **4T-Ir**. As demonstrated in Supporting Information Figures S32−S36 for the ***n*T-Ir**, all complexes produced singlet oxygen and peroxynitrite anions and **1T-Ir**−**4T-Ir** also generated superoxide anion radicals upon cool white light irradiation with and without SKMEL28 cells, and the presence of scavengers for these ROS species either suppressed the generation of these species or reduced their photocytotoxicity. In contrast, no hydroxyl radicals or hydrogen peroxide were generated from these complexes upon photoactivation, which was confirmed by the lack of impact on the cell viability upon the addition of scavengers for these two species. The results of these collective experiments indicate that singlet oxygen, superoxide anion radicals, and peroxynitrite anions could be involved in photocytotoxicity, while hydroxyl radicals and hydrogen peroxide do not appear to be involved.

It should be noted that these RMS represent only a handful of possibilities and should be interpreted with caution. Oligothiophenes are known to exhibit complex redox behavior, and it is likely that a combination of primary and competing phototoxic pathways operates in tandem and could in fact be followed by secondary chain reactions. The fact that the most potent compounds are subject to photobleaching yet are extremely active underscores that there is much still to be learned and that the source of photocytotoxicity should not be viewed in terms of one exclusive pathway. In addition, the variation in activity within and across cell lines could reflect different mechanistic pathways or contributions but could also simply reflect differences in melanocytic activity since melanin


https://doi.org/10.1021/acs.inorgchem.4c03847
Inorg. Chem. 2024, 63, 21323−21335

is known to detoxify RMS but can also contribute to a source of oxidative stress.[56]

The complexes were also tested for their abilities to be selectively phototoxic toward cancer cell lines compared with noncancerous skin fibroblast cells (CCD-1064Sk). As shown in Supporting Information Table S6, the complexes did not exhibit any selectivity for cancer cells over noncancerous cells, underscoring the importance of light as a means to control where and when the compounds are cytotoxic.

## CONCLUSIONS

Five tricationic bis-tpy Ir(III) complexes bearing varying oligothiophene units ***n*T-Ir** ($n$ = 0−4) on one of the tpy ligands were synthesized and fully characterized. Systematical photophysical studies of the $Cl^-$ salts of these complexes revealed that oligothienyl substitution introduced ***n*T-tpy** localized $\pi,\pi^*$/ILCT configurations into the lowest singlet and triplet excited states, which caused red-shifts of the lowest-energy absorption bands and emission bands. Increasing the number of thienyl units from 0 to 4 progressively shifted the $^1\pi,\pi^*/^1$CT absorption bands from the UV region in **0T-Ir** to green/orange spectral regions in **4T-Ir** and the emission bands bathochromically shifted from blue/green to the NIR regions. In contrast, the $T_1$ lifetimes increased from **0T-Ir** to **2T-Ir** but decreased in **3T-Ir** and **4T-Ir**, reflecting the overplay of the increased $^3\pi,\pi^*/^3$ILCT contribution in $T_1$ and the enhanced nonradiative decay rates associated with the reduced $T_1$ energies when the number of thienyl units increased. In accordance with the trend observed for the $T_1$ lifetimes, the singlet oxygen generation efficiency ($\Phi_\Delta$) also followed the same trend, which consequently impacted the trend of the *in vitro* photocytotoxicity toward SKMEL28, MDA-MB-231, and MCF-7 cells upon visible, blue, and green light activation under normoxia. However, for B16F10 and A375 cells, **4T-Ir** exhibited the strongest PDT effects followed by **2T-Ir** and then **3T-Ir** under normoxia regardless of the excitation light wavelengths. Upon red-light excitation, **4T-Ir** also showed the strongest PDT effects compared to those of the other four complexes toward all cell lines under normoxia. More importantly, **4T-Ir** retained its photocytotoxicity under hypoxia toward all cell lines upon visible, blue, and green light excitation, suggesting the importance of increasing the number of thienyl groups on the tpy ligand. In addition to singlet oxygen, superoxide anion radicals, and peroxynitrite anions were found to likely be involved in the photocytotoxicity exhibited by the complexes. The hypoxic activity, together with the red-shifted absorption and emission and low dark cytotoxicity, makes the **4T-Ir** complex a potential hypoxia-active PS for PDT application. To further red-shift the absorption of this complex to the biologically relevant NIR range, the complex could be tethered to a $\pi$-conjugated organic chromophore such as the styryl-substituted BODIPY like we reported for a neutral Ir(III) complex **BODIPY-Ir** before.[19] To improve the aqueous solubility of these complexes, carboxylate, sulfonate, or quaternary ammonium substituents could be introduced to one or both tpy ligands and to the *n*T groups. Alternatively, the current complexes could be encapsulated into micelles or nanovehicles formed by amphiphilic polymers. These strategies will be investigated and utilized in our future work.

## ASSOCIATED CONTENT

### Supporting Information

The Supporting Information is available free of charge at https://pubs.acs.org/doi/10.1021/acs.inorgchem.4c03847.

The 1D and 2D $^1$H NMR spectra of **0T-Ir−4T-Ir** in DMSO-$d_6$ and $CD_3OD$, 1D $^{13}$C NMR spectra of **0T-Ir−4T-Ir** in DMSO-$d_6$, high-resolution mass spectra and HPLC traces of **0T-Ir−4T-Ir**; dark and photostability of **2T-Ir − 4T-Ir** in $H_2O$/DMSO solution; comparison of the experimental and calculated absorption spectra of **0T-Ir−4T-Ir** in methanol; NTOs of the major transitions contributing to the high-energy absorption bands for **0T-Ir−4T-Ir** in methanol; normalized UV−vis absorption spectra of **2T-Ir−4T-Ir** in different solvents; UV−vis absorption spectra of **4T-Ir** in mixed DMSO/$H_2O$; the emission spectra of ligands **2T-tpy − 4T-tpy**; the calculated emission spectra and MOs of **0T-Ir − 4T-Ir** in methanol; the excitation spectra of **0T-Ir−4T-Ir** in methanol at r.t. and 77 K; the $EC_{50}$ values of **0T-Ir−4T-Ir** toward MDA-MB-231 and MCF-7 cells under normoxia and hypoxia; and the RMS measurements for **0T-Ir−4T-Ir** with and without the SKMEL28 cells (PDF)

## AUTHOR INFORMATION


### Corresponding Authors

**Wenfang Sun** − *Department of Chemistry and Biochemistry, The University of Alabama, Tuscaloosa, Alabama 35487-0336, United States;* orcid.org/0000-0003-3608-611X; Phone: 205-348-5807; Email: wsun15@ua.edu

**Sherri A. McFarland** − *Department of Chemistry and Biochemistry, The University of Texas at Arlington, Arlington, Texas 76019-0065, United States;* orcid.org/0000-0002-8028-5055; Phone: 817-272-6068; Email: sherri.mcfarland@uta.edu

### Authors

**Xinyang Sun** − *Department of Chemistry and Biochemistry, The University of Alabama, Tuscaloosa, Alabama 35487-0336, United States*

**Houston D. Cole** − *Department of Chemistry and Biochemistry, The University of Texas at Arlington, Arlington, Texas 76019-0065, United States;* orcid.org/0000-0002-2922-2163

**Ge Shi** − *Department of Chemistry and Biochemistry, The University of Texas at Arlington, Arlington, Texas 76019-0065, United States*

**Victoria Oas** − *Department of Chemistry and Biochemistry, North Dakota State University, Fargo, North Dakota 58108-6050, United States;* orcid.org/0009-0000-3583-9904

**Alisher Talgatov** − *Department of Chemistry and Biochemistry, The University of Texas at Arlington, Arlington, Texas 76019-0065, United States;* orcid.org/0000-0002-9421-6878

**Colin G. Cameron** − *Department of Chemistry and Biochemistry, The University of Texas at Arlington, Arlington, Texas 76019-0065, United States;* orcid.org/0000-0003-0978-0894

**Svetlana Kilina** − *Department of Chemistry and Biochemistry, North Dakota State University, Fargo, North Dakota 58108-6050, United States;* orcid.org/0000-0003-1350-2790

Complete contact information is available at:

https://pubs.acs.org/10.1021/acs.inorgchem.4c03847

### Author Contributions

†X.S. and H.D.C. contributed equally to this work.

### Notes

The authors declare the following competing financial interest(s): S.A.M. has a potential research conflict of interest due to a financial interest with Theralase Technologies, Inc. and PhotoDynamic, Inc. A management plan has been created to preserve objectivity in research in accordance with UTA policy. The other authors declare no competing financial interest.

## ■ ACKNOWLEDGMENTS

W. S. and S.A.M. acknowledge the financial support from National Science Foundation (DMR-2317606 and DMR-2004971) for photosensitizer synthesis, photophysical studies, and photobiological studies. S.K. would like to thank the Department of Energy (DE-SC0022239) for supporting the computational part of the work. S.A.M. thanks Dr. Brian Edwards (UTA) for his experimental support and instrument maintenance as NMR facility manager. S.A.M acknowledges the Texas Advanced Computing Center (TACC) at The University of Texas at Austin for providing storage resources that have contributed to the research results reported within this paper.

## ■ REFERENCES

(1) Kalyanasundaram, K.; Grätzel, M. Applications of functionalized transition metal complexes in photonic and optoelectronic devices. *Coord. Chem. Rev.* **1998**, *177*, 347−414.
(2) Choy, W. C. H.; Chan, W. K.; Yuan, Y. Recent Advances in Transition Metal Complexes and Light-Management Engineering in Organic Optoelectronic Devices. *Adv. Mater.* **2014**, *26*, 5368−5399.
(3) Xu, H.; Chen, R.; Sun, Q.; Lai, W.; Su, Q.; Huang, W.; Liu, X. Recent Progress in Metal−Organic Complexes for Optoelectronic Applications. *Chem. Soc. Rev.* **2014**, *43*, 3259−3302.
(4) Lv, Q.; Yu, R.; Shi, R.; Tan, Z. Recent Progress in Organic-Metal Complexes for Organic Photovoltaic Applications. *Mater. Chem. Front.* **2023**, *7*, 5063−5103.
(5) Wegeberg, C.; Wenger, O. S. Luminescent First-Row Transition Metal Complexes. *JACS Au* **2021**, *1*, 1860−1876.
(6) Prier, C. K.; Rankic, D. A.; MacMillan, W. C. Visible Light Photoredox Catalysis with Transition Metal Complexes: Applications in Organic Synthesis. *Chem. Rev.* **2013**, *113*, 5322−5363.
(7) Mari, C.; Pierroz, V.; Ferrari, S.; Gasser, G. Combination of Ru(II) Complexes and Light: New Frontiers in Cancer Therapy. *Chem. Sci.* **2015**, *6*, 2660−2686.
(8) Stacey, O. J.; Pope, S. J. A. New Avenues in the Design and Potential Application of Metal Complexes for Photodynamic Therapy. *RSC Adv.* **2013**, *3*, 25550−25564.
(9) McFarland, S. A.; Mandel, A.; Dumoulin-White, R.; Gasser, G. Metal-Based Photosensitizers for Photodynamic Therapy: The Future of Multimodal Oncology? *Curr. Opin. Chem. Biol.* **2020**, *56*, 23−27.
(10) Monro, S.; Colón, K. L.; Yin, H.; Roque, J., III; Konda, P.; Gujar, S.; Thummel, R. P.; Lilge, L.; Cameron, C. G.; McFarland, S. A. Transition Metal Complexes and Photodynamic Therapy from a Tumor-Centered Approach: Challenges, Opportunities, and Highlights from the Development of TLD1433. *Chem. Rev.* **2019**, *119*, 797−828.
(11) Imberti, C.; Zhang, P.; Huang, H.; Sadler, P. J. New Designs for Phototherapeutic Transition Metal Complexes. *Angew. Chem., Int. Ed.* **2020**, *59*, 61−73.
(12) Zamora, A.; Vigueras, G.; Rodríguez, V.; Santana, M. D.; Ruiz, J. Cyclometalated Iridium(III) Luminescent Complexes in Therapy and Phototherapy. *Coord. Chem. Rev.* **2018**, *360*, 34−76.
(13) Jing, S.; Wu, X.; Niu, D.; Wang, J.; Leung, C.-H.; Wang, W. Recent Advances in Organometallic NIR Iridium(III) Complexes for Detection and Therapy. *Molecules* **2024**, *29*, 256.
(14) Huang, H.; Banerjee, S.; Sadler, P. J. Recent Advances in the Design of Targeted Iridium(III) Photosensitizers for Photodynamic Therapy. *ChemBioChem.* **2018**, *19*, 1574−1589.
(15) Huang, T.; Yu, Q.; Liu, S.; Huang, W.; Zhao, Q. Phosphorescent Iridium(III) Complexes: A Versatile Tool for Biosensing and Photodynamic Therapy. *Dalton Trans.* **2018**, *47*, 7628−7633.
(16) Juris, A.; Balzani, V.; Barigelletti, F.; Campagna, S.; Belser, P.; von Zelewsky, A. Ru(II) Polypyridine Complexes: Photophysics, Photochemistry, Electrochemistry, and Chemiluminescence. *Coord. Chem. Rev.* **1988**, *84*, 85−277.
(17) Novohradsky, V.; Rovira, A.; Hally, C.; Galindo, A.; Vigueras, G.; Gandioso, A.; Svitelova, M.; Bresolí-Obach, R.; Kostrhunova, H.; Markova, L.; Kasparkova, J.; Nonell, S.; Ruiz, J.; Brabec, V.; Marchán, V. Towards Novel Photodynamic Anticancer Agents Generating Superoxide Anion Radicals: A Cyclometalated $Ir^{III}$ Complex Conjugated to a Far-Red Emitting Coumarin. *Angew. Chem., Int. Ed.* **2019**, *58*, 6311−6315.
(18) Zhao, J.; Yan, K.; Xu, G.; Liu, X.; Zhao, Q.; Xu, C.; Gou, S. An Iridium(III) Complex Bearing a Donor−Acceptor−Donor Type Ligand for NIR-Triggered Dual Phototherapy. *Adv. Funct. Mater.* **2020**, *31*, No. 2008325.
(19) Liu, B.; Jiao, J.; Xu, W.; Zhang, M.; Cui, P.; Guo, Z.; Deng, Y.; Chen, H.; Sun, W. Highly Efficient Far-Red/NIR-Absorbing Neutral Ir(III) Complex Micelles for Potent Photodynamic/Photothermal Therapy. *Adv. Mater.* **2021**, *33*, No. 2100795.
(20) Yang, Q.; Jin, H.; Gao, Y.; Lin, J.; Yang, H.; Yang, S. Photostable Iridium(III)-Cyanine Complex Nanoparticles for Photoacoustic Imaging Guided Near-Infrared Photodynamic Therapy in Vivo. *ACS Appl. Mater. Interfaces* **2019**, *11*, 15417−15425.
(21) Lee, S. Y.; Kim, C. A.-O.; Nam, T. A.-O. Ruthenium Complexes as Anticancer Agents: A Brief History and Perspectives. *Drug Des. Devel. Ther.* **2020**, *14*, 5375−5392.
(22) Svensson, F. R.; Abrahamsson, M.; Strömberg, N.; Ewing, A. G.; Lincoln, P. Ruthenium(II) Complex Enantiomers as Cellular Probes for Diastereomeric Interactions in Confocal and Fluorescence Lifetime Imaging Microscopy. *J. Phys. Chem. Lett.* **2011**, *2*, 397−401.
(23) Haq, I.; Lincoln, P.; Suh, D.; Norden, B.; Chowdhry, B. Z.; Chaires, J. B. Interaction of Δ- and Λ-$[Ru(phen)_2DPPZ]^{2+}$ with DNA: A Calorimetric and Equilibrium Binding Study. *J. Am. Chem. Soc.* **1995**, *117*, 4788−4796.
(24) Huang, R.; Feng, F.-P.; Huang, C.-H.; Mao, L.; Tang, M.; Yan, Z.-Y.; Shao, B.; Qin, L.; Xu, T.; Xue, Y.-H.; Zhu, B.-Z. Chiral Os(II) Polypyridyl Complexes as Enantioselective Nuclear DNA Imaging Agents Especially Suitable for Correlative High-Resolution Light and Electron Microscopy Studies. *ACS Appl. Mater. Interfaces* **2020**, *12*, 3465−3473.
(25) Chao, X.-J.; Huang, C.-H.; Tang, M.; Yan, Z.-Y.; Huang, R.; Li, Y.; Zhu, B.-Z. Unusual Enantioselective Cytoplasm-to-Nucleus Translocation and Photosensitization of the Chiral Ru(II) Cationic Complex via Simple Ion Pairing with Lipophilic Weak Acid Counter-Anions. *Nucleic Acids Res.* **2023**, *51*, 3041−3054.
(26) Tamayo, A.; Alleyne, B.; Djurovich, P. I.; Lamansky, S.; Tsyba, I.; Ho, N.; Bau, R.; Thompson, M. E. Synthesis and Characterization of Facial and Meridional Tris-cyclometalated Iridium(III) Complexes. *J. Am. Chem. Soc.* **2003**, *125*, 7377−7387.
(27) Shi, C.; Sun, H.; Tang, X.; Lv, W.; Yan, H.; Zhao, Q.; Wang, J.; Huang, W. Variable Photophysical Properties of Phosphorescent Iridium(III) Complexes Triggered by closo- and nido-Carborane Substitution. *Angew. Chem., Int. Ed.* **2013**, *52*, 13434−13438.
(28) Lu, C.; Xu, W.; Shah, H.; Liu, B.; Xu, W.; Sun, L.; Qian, S. Y.; Sun, W. *In vitro* Photodynamic Therapy of Mononuclear and Dinuclear Iridium(III) Bis(terpyridine) Complexes. *ACS Appl. Bio Mater.* **2020**, *3*, 6865−6875.
(29) Liu, B.; Monro, S.; Li, Z.; Jabed, M. A.; Ramirez, D.; Cameron, C. G.; Colon, K.; Roque, J., III; Kilina, S.; Tian, J.; McFarland, S. A.;

Sun, W. A New Class of Homoleptic and Heteroleptic Bis-(terpyridine) Iridium(III) Complexes with Strong Photodynamic Therapy Effects. *ACS Appl. Bio Mater.* **2019**, *2*, 2964−2977.
(30) Liu, B.; Monro, S.; Lystrom, L.; Cameron, C. G.; Colon, K.; Yin, H.; Kilina, S.; McFarland, S. A.; Sun, W. Photophysical and Photobiological Properties of Dinuclear Iridium(III) Bis-tridentate Complexes. *Inorg. Chem.* **2018**, *57*, 9859−9872.
(31) Xu, W.; Lystrom, L.; Pan, Y.; Sun, X.; Thomas, S. A.; Kilina, S.; Yang, Z.; Wang, H.; Hobbie, E.; Sun, W. Mono-/Bi-metallic Neutral Iridium(III) Complexes Bearing Diketopyrrolopyrrole−Substituted *N*−Heterocyclic Carbene (NHC) Ligands: Synthesis and Photophysics. *Inorg. Chem.* **2021**, *60*, 15278−15290.
(32) Liu, B.; Monro, S.; Jabed, M. A.; Cameron, C. G.; Colón, K. L.; Xu, W.; Kilina, S.; McFarland, S. A.; Sun, W. Neutral iridium(III) complexes bearing BODIPY−substituted N−heterocyclic carbene (NHC) ligands: synthesis, photophysics, in vitro theranostic photodynamic therapy, and antimicrobial activity. *Photochem. Photobiol. Sci.* **2019**, *18*, 2381−2396.
(33) Liu, B.; Gao, Y.; Jabed, M. A.; Kilina, S.; Liu, G.; Sun, W. Lysosome-Targeting Bis-terpyridine Ruthenium(II) Complexes: Photophysical Properties and in vitro Photodynamic Activities. *ACS Appl. Bio Mater.* **2020**, *3*, 6025−6038.
(34) Shi, G.; Monro, S.; Hennigar, R.; Colpitts, J.; Fong, J.; Kasimova, K.; Yin, H.; DeCoste, R.; Spencer, C.; Chamberlain, L.; Mandel, A.; Lilge, L.; McFarland, S. A. Ru(II) Dyads Derived from α-Oligothiophenes: A New Class of Potent and Versatile Photosensitizers for PDT. *Coord. Chem. Rev.* **2015**, *282*−*283*, 127−138.
(35) Monro, S.; Cameron, C. G.; Zhu, X.; Colón, K. L.; Yin, H.; Sainuddin, T.; Hetu, M.; Pinto, M.; Fuller, A.; Bennett, L.; Roque, J., III; Sun, W.; McFarland, S. A. Synthesis, Characterization and Photobiological Studies of Ru(II) Dyads Derived from α-Oligothiophene Derivatives of 1,10-Phenanthroline. *Photochem. Photobiol.* **2019**, *95*, 267−279.
(36) Roque, J. A., III; Cole, H. D.; Barrett, P. C.; Lifshits, L. M.; Hodges, R. O.; Kim, S.; Deep, G.; Francés-Monerris, A.; Alberto, M. E.; Cameron, C. G.; McFarland, S. A. Intraligand Excited States Turn a Ruthenium Oligothiophene Complex into a Light-Triggered Ubertoxin with Anticancer Effects in Extreme Hypoxia. *J. Am. Chem. Soc.* **2022**, *144*, 8317−8336.
(37) Cole, H. D.; Roque, J. A., III; Shi, G.; Lifshits, L. M.; Ramasamy, E.; Barrett, P. C.; Hodges, R. O.; Cameron, C. G.; McFarland, S. A. Anticancer Agent with Inexplicable Potency in Extreme Hypoxia: Characterizing a Light-Triggered Ruthenium Ubertoxin. *J. Am. Chem. Soc.* **2022**, *144*, 9543−9547.
(38) Cole, H. D.; Vali, A.; Roque, J. A., III; Shi, G.; Kaur, G.; Hodges, R. O.; Francés-Monerris, A.; Alberto, M. E.; Cameron, C. G.; McFarland, S. A. Ru(II) Phenanthroline-Based Oligothienyl Complexes as Phototherapy Agents. *Inorg. Chem.* **2023**, *62*, 21181−21200.
(39) Yilmaz, M.; Erkartal, M.; Ozdemir, M.; Sen, U.; Usta, H.; Demirel, G. Three-Dimensional Au-Coated Electrosprayed Nanostructured BODIPY Films on Aluminum Foil as Surface-Enhanced Raman Scattering Platforms and Their Catalytic Applications. *ACS Appl. Mater. Interfaces* **2017**, *9*, 18199−18206.
(40) Ghosh, G.; Colón, K. L.; Fuller, A.; Sainuddin, T.; Bradner, E.; McCain, J.; Monro, S. M.; Yin, H.; Hetu, M. W.; Cameron, C. G.; McFarland, S. A. Cyclometalated Ruthenium(II) Complexes Derived from α-Oligothiophenes as Highly Selective Cytotoxic or Photocytotoxic Agents. *Inorg. Chem.* **2018**, *57*, 7694−7712.
(41) Paisley, N. R.; Tonge, C. M.; Sauvé, E. R.; Halldorson, S. V.; Hudson, Z. M. Synthesis of Polymeric Organic Semiconductors Using Semifluorinated Polymer Precursors. *J. Polym. Sci. A: Polym. Chem.* **2018**, *56*, 2183−2191.
(42) Chen, R.; Yang, X.; Tian, H.; Wang, X.; Hagfeldt, A.; Sun, L. Effect of Tetrahydroquinoline Dyes Structure on the Performance of Organic Dye-Sensitized Solar Cells. *Chem. Mater.* **2007**, *19*, 4007−4015.
(43) DeRosa, M. C.; Crutchley, R. J. Photosensitized Singlet Oxygen and Its Applications. *Coord. Chem. Rev.* **2002**, *233*−*234*, 351−371.
(44) Frisch, M. J.; Trucks, G. W.; Schlegel, H. B.; Scuseria, G. E.; Robb, M. A.; Cheeseman, J. R.; Scalmani, G.; Barone, V.; Petersson, G. A.; Nakatsuji, H.; Li, X.; Caricato, M.; Marenich, A. V.; Bloino, J.; Janesko, B. G.; Gomperts, R.; Mennucci, B.; Hratchian, H. P.; Ortiz, J. V.; Izmaylov, A. F.; Sonnenberg, J. L.; Williams-Young, D.; Ding, F.; Lipparini, F.; Egidi, F.; Goings, J.; Peng, B.; Petrone, A.; Henderson, T.; Ranasinghe, D.; Zakrzewski, V. G.; Gao, J.; Rega, N.; Zheng, G.; Liang, W.; Hada, M.; Ehara, M.; Toyota, K.; Fukuda, R.; Hasegawa, J.; Ishida, M.; Nakajima, T.; Honda, Y.; Kitao, O.; Nakai, H.; Vreven, T.; Throssell, K.; Montgomery, J. A., Jr.; Peralta, J. E.; Ogliaro, F.; Bearpark, M. J.; Heyd, J. J.; Brothers, E. N.; Kudin, K. N.; Staroverov, V. N.; Keith, T. A.; Kobayashi, R.; Normand, J.; Raghavachari, K.; Rendell, A. P.; Burant, J. C.; Iyengar, S. S.; Tomasi, J.; Cossi, M.; Millam, J. M.; Klene, M.; Adamo, C.; Cammi, R.; Ochterski, J. W.; Martin, R. L.; Morokuma, K.; Farkas, O.; Foresman, J. B.; Fox, D. J. *Gaussian16*, Revision B.01, Gaussian, Inc.: Wallingford CT, 2016.
(45) Kohn, W.; Sham, L. J. Self-Consistent Equations Including Exchange and Correlation Effects. *Phys. Rev.* **1965**, *140*, A1133−A1138.
(46) Casida, M. E.; Jamorski, C.; Casida, K. C.; Salahub, D. R. Molecular Excitation Energies to High-Lying Bound States from Time-Dependent Density-Functional Response Theory: Characterization and Correction of the Time-Dependent Local Density Approximation Ionization Threshold. *J. Chem. Phys.* **1998**, *108*, 4439−4449.
(47) Hay, P. J.; Wadt, W. R. Ab Initio Effective Core Potentials for Molecular Calculations. Potentials for the Transition Metal Atoms Sc to Hg. *J. Chem. Phys.* **1985**, *82*, 270−283.
(48) Clark, T.; Chandrasekhar, J.; Spitznagel, G. W.; Schleyer, P. V. R. Efficient Diffuse Function-Augmented Basis Sets for Anion Calculations. III. The 3-21+G Basis Set for First-Row Elements, Li−F. *J. Comput. Chem.* **1983**, *4*, 294−301.
(49) Gill, P. M. W.; Johnson, B. G.; Pople, J. A.; Frisch, M. J. The Performance of the Becke-Lee-Yang-Parr (B-LYP) Density Functional Theory with Various Basis Sets. *Chem. Phys. Lett.* **1992**, *197*, 499−505.
(50) Adamo, C.; Barone, V. Toward Reliable Density Functional Methods without Adjustable Parameters: The PBE0Model. *J. Chem. Phys.* **1999**, *110*, 6158−6170.
(51) Barone, V.; Cossi, M.; Tomasi, J. Geometry Optimization of Molecular Structures in Solution by the Polarizable Continuum Model. *J. Comput. Chem.* **1998**, *19*, 404−417.
(52) Martin, R. L. Natural Transition Orbitals. *J. Chem. Phys.* **2003**, *118*, 4775−4777.
(53) Neese, F. Software Update: the ORCA Program System - Version 5.0. *Wiley Interdiscip. Rev.: Comput. Mol. Sci.* **2022**, *12*, No. e1606.
(54) Rolfes, J. D.; Neese, F.; Pantazis, D. A. All-Electron Scalar Relativistic Basis Sets for the Elements Rb−Xe. *J. Comput. Chem.* **2020**, *41*, 1842−1849.
(55) Bopp, S. K.; Lettieri, T. Comparison of Four Different Colorimetric and Fluorometric Cytotoxicity Assays in a Zebrafish Liver Cell Line. *BMC Pharmacol.* **2008**, *8*, 8.
(56) Diehl, C. Melanocytes and Oxidative Stress. *J. Pigm. Disord.* **2014**, *1*, No. 100127.


https://doi.org/10.1021/acs.inorgchem.4c03847
*Inorg. Chem.* 2024, 63, 21323−21335